Published on
Mineralogy and Petrology (2018) 112:555 – 576
https://doi.org/10.1007/s00710-017-0542-y

The influence of petrography, mineralogy and chemistry on burnability and reactivity of quicklime produced in Twin Shaft Regenerative (TSR) kilns from Neoarchean limestone (Transvaal Supergroup, South Africa)

Gabriele Vola[1,2] · Luca Sarandrea[1] · Giovanna Della Porta[3] · Alessandro Cavallo[4] · Flavio Jadoul[3] · Giuseppe Cruciani[2]

Abstract

This study evaluates the influence of chemical, mineralogical and petrographic features of the Neoarchean limestone from the Ouplaas Mine (Griqualand West, South Africa) on its burnability and quicklime reactivity, considering the main use as raw material for high-grade lime production in twin shaft regenerative (TSR) kilns. This limestone consists of laminated clotted peloidal micrite and fenestrate microbial boundstone with herringbone calcite and organic carbon (kerogen) within stylolites. Diagenetic modifications include hypidiotopic dolomite, micrite to microsparite recrystallization, stylolites, poikilotopic calcite, chert and saddle dolomite replacements. Burning and technical tests widely attest that the Neoarchean limestone is sensitive to high temperature, showing an unusual and drastically pronounced sintering or overburning tendency. The slaking reactivity, according to EN 459-2 is high for lime burnt at 1050 °C, but rapidly decreases for lime burnt at 1150 °C. The predominant micritic microbial textures, coupled with the organic carbon, are key-factors influencing the low burnability and the high sintering tendency. The presence of burial cementation, especially poikilotopic calcite, seems to promote higher burnability, either in terms of starting calcination temperature, or in terms of higher carbonate dissociation rate. In fact, the highest calcination velocity determined by thermal analysis is consistent with the highest slaking reactivity of the lower stratum of the quarry, enriched in poikilotopic calcite. Secondly, locally concentered dolomitic marly limestones, and sporadic back shales negatively affects the quicklime reactivity, as well. This study confirms that a multidisciplinary analytical approach is essential for selecting the best raw mix for achieving the highest lime reactivity in TSR kilns.

Introduction

This research investigates the influence of texture, microstructure, mineralogy, and bulk rock chemistry of Neoarchean limestone (Transvaal Supergroup, South Africa) on its thermal behavior and burnability for the production of industrial high reactive quicklime. The traditional calcination models for rotary and vertical shaft kilns (Boynton 1980; Cheng and Specht 2006) have recently been revisited. These revised calcination processes take into account not only the carbonate chemistry and mineralogy (Marinoni et al. 2012), but also the effect of the limestone microfacies and microstructure, resulting from depositional processes and early to late diagenetic modifications (Moropoulou et al. 2001; Kiliç and Mesut 2006; Hughes and Corrigan 2009;

[1] Cimprogetti S.r.l., via Pasubio, 5, 24044 Dalmine, Italy

[2] Department of Physics and Earth Sciences, University of Ferrara, Via Saragat, 1, 44122 Ferrara, Italy

[3] Department of Earth Sciences "Ardito Desio", University of Milan, Via Mangiagalli, 34, 20133 Milano, Italy

[4] Department of Earth and Environmental Sciences, University of Milano-Bicocca, Piazza dell'Ateneo Nuovo, 1, 20126 Milano, Italy

Vola and Sarandrea 2013; Marinoni et al. 2015). Studies on

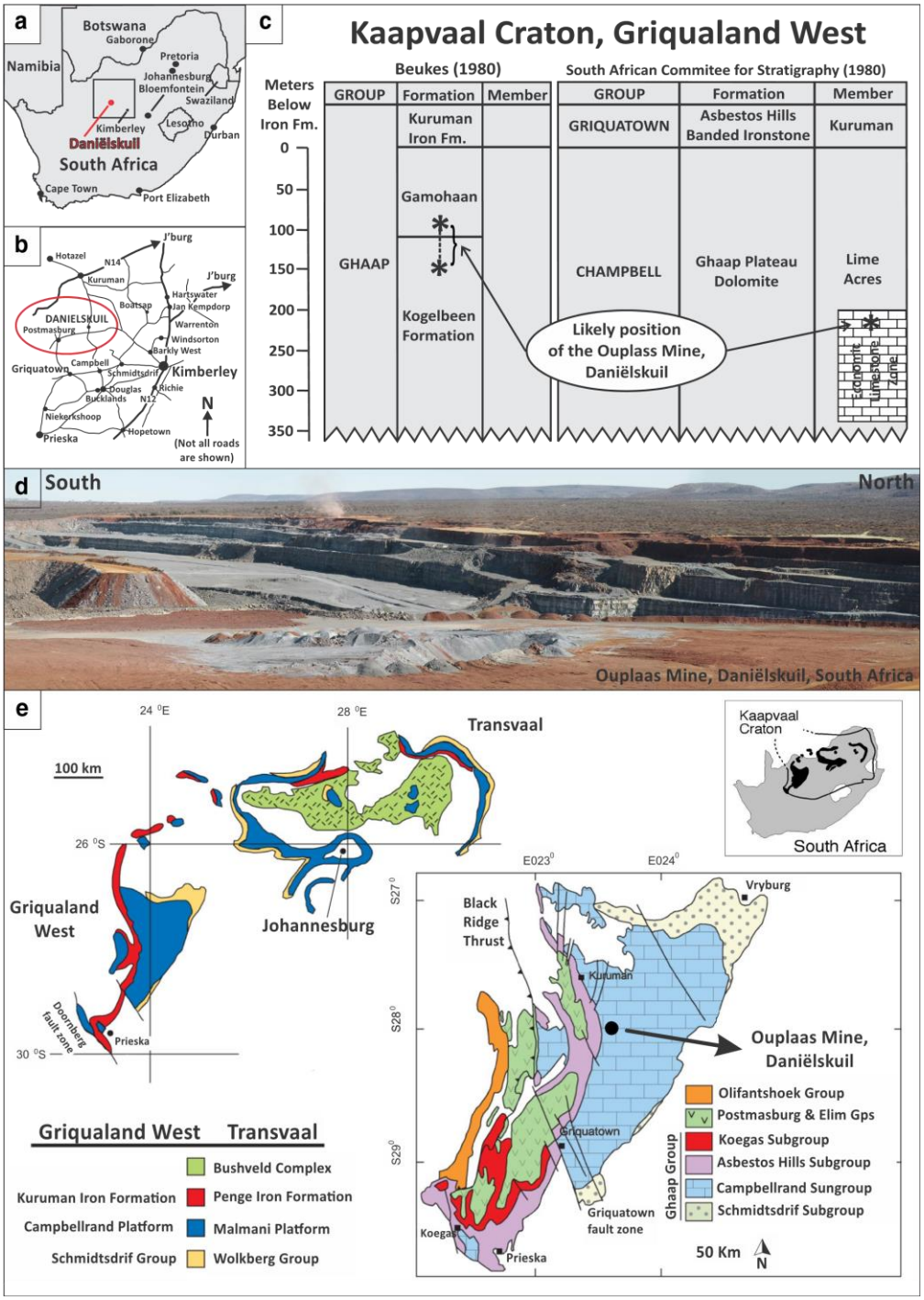

Fig. 1 **a-b** Location of the investigated Ouplass Mine. **c** Simplified stratigraphic columns for a portion of the Transvaal Supergroup of the Kaapvaal Craton in the Griqualand West Basin, according to Beukes (1980) and SACS (1980) (modified after Altermann and Schopf 1995). **d** Landscape photograph of bench 4P and 4S of the Ouplass Mine. **e** Simplified geological map of the Kaapvaal Craton, showing the Late Archean Transvaal Supergroup, broadly divided into two structural sub-basins. The inset contains a detailed close-up map of the stratigraphic units in Griqualand West, South Africa (modified after Paris et al. 2014)

mud-supported and grain-supported limestones from Egypt (Soltan 2009; Soltan et al. 2011, 2012) and the United Arab Emirates (Alaabed et al. 2014) demonstrated the impact of different microfacies types and their related open porosity, on the quality of the high-calcium lime, as well as, other compositional and process parameters. The limestone microstructure plays a key role in controlling the calcination activation energy (Soltan and Serry 2011; Marinoni et al. 2015). Other recent and important studies treat the influence of mineralogy, petrography and microstructure on the thermal decomposition of limestone used for the Portland cement clinker production (Marinoni et al. 2015; Galimberti et al. 2016).

The main goal of this study is to present an industrial case study, by investigating issues related to reaching the target quality of the lime product in Twin Shaft Regenerative (TSR) kilns. Furthermore, this study also attempts to improve the knowledge on burnability and lime reactivity of an ancient microbial limestone, affected by exceptionally long and pervasive diagenesis, and showing an unusual heating behavior with a low burnability associated with an evident sintering tendency at 1150 °C.

The Lime Operation at Ouplaas Mine, near Daniëlskuil in the Northern Cape Province, South Africa (Fig. 1), entails the mining of high-grade calcium carbonate of Neoarchean age, crushing, screening, burning, and milling in the production of limestone aggregate, filler, and burnt lime, as well as a hydration facility for the production of slaked lime. Idwala Lime commissioned two modern energy efficient Cimprogetti's double TSR kilns with a capacity of 550 TPD in 2011. The first kiln (K9) was erected in September 2013, and the second (K10) in February 2014. Significant issues were identified during the kiln start-up in the early stage of production and regarded either the low reactivity, or the high residual CO_2 content of the lime. Moreover, lumps of burnt lime observed at the discharging drawers of the kiln presented an evident variability of color, ranging from light brown (5YR 6/4) to pale brown (5YR 5/2), and medium dark gray (N4), according to the Geological Munsell Rock-color chart (Table 1). Primarily, the color inhomogeneity was explained as due to different oxidation states, namely significant inhomogeneous distribution of the heat flow within the kiln section, because of the different residual CO_2 content.

Secondary, the visual inspection of limestone aggregates transported over the conveyor belt to the stockpile allowed identifying at least two or three main different lithofacies types, which could affect the final quality of the lime. During the six-month period of the commissioning phase, different process parameters were controlled, and the production of both kilns was stabilized. The target of a low residual CO_2 content (< 2%) was easily matched; on the contrary the slaking reactivity did not reach the expected (t_{60} < 2 min.), according to the EN 459-2 standard test method (Table 1, Vola and Sarandrea 2014).

Hence, limestone samples from different benches of the mine, namely 2P, 4P and 4S, were sampled by the client and sent to Cimprogetti laboratory, to evaluate their compositional, i.e. chemical and mineralogical, microstructural and petrographic features, the thermal behavior, and the burnability at different temperatures, to simulate different combustion conditions in TSR kilns. Data collection described the unusual burnability of the Neoarchean limestone, and allowed identifying its sintering or overburning tendency, which seems to be controlled by the pervasive micrite/microsparite distribution within the primary microbial carbonate texture combined with the presence of abundant organic carbon (kerogen), which also burns during the calcination process. Moreover, the uneven distribution of non-carbonate impurity, essentially clay minerals and pyrite, negatively affects the reactivity and the available lime index.

Taking into account the mine stratigraphy (Fig. 2) and the lime reactivity of different strata, it was possible to calculate the average weighted reactivity of each bench and, subsequently, the expected reactivity of different raw mixes feeding to the kilns. This multidisciplinary research demonstrates that the judicious selection of raw materials from the mine significantly improves the quality control of the quicklime production and that it is good practice selecting the best raw mix to feed to stockpiles and kilns. This step must be considered of primary importance, as well as the fine tuning of different process parameters (cf. Vola and Sarandrea 2014).

Geological setting

The limestone quarried at the Ouplaas Mine in Daniëlskuil, Griqualand West, northern Cape Province, South Africa, belongs to the "Economic Limestone Zone" of the Lime Acres Member of the Ghaap Plateau Dolomite Fm. according to SACS (1980), whereas according to Beukes (1980) this limestone represents the uppermost part of the Kogelbeen Fm. / the lower part of the Gamohaan Fm. The Ouplaas Mine limestone is part of the Neoarchean Campbellrand-Malmani platform, which represents one of the oldest carbonate shelves (2521 ± 3 Ma according to Sumner and

Table 1 Results of preliminary technical tests performed on burnt lime samples from the industrial plant (Vola and Sarandrea 2014)

Burnt state	Unit	Soft	Medium	Hard
Munsell rock-color		light brown	pale brown	medium dark gray
Residual CO_2	Wt. %	2.8	1.7	1.3
Reactivity (t_{60})	min	1.01	11.43	NR
Reactivity (T_{max})	°C	70.00	61.6	41.7
Available lime index	Wt.%	94.5	92.9	89.7
BET specific surface area	m^2/g	4.0	1.4	0.35
Mercury intrusion porosity	Wt.%	47.62	41.89	32.18
Average pore radius	µm	0.31	0.52	1.33

Symbols legend: NR = t_{60} not reached

Bowring 1996) with microbialites and stromatolites preserved worldwide (Grotzinger 1989; Grotzinger and James 2000). The Campbell Group carbonates are host to many economically important mineral deposits in the Northern Cape Province (Altermann and Wotherspoon 1995). The eastern part of the platform is traditionally called Transvaal Basin, whereas the western part is called Griqualand West Basin (Fig. 1).

From a structural point of view, the Campbellrand-Malmani carbonate platform (Fig. 1e) is extremely well preserved. Undated tectonic events are limited to gentle warping over most of the craton with locally steeper dips around the Bushveld Complex in the North and to intense folding and faulting in the Kheis Belt and Dooringberg Fault Zone, which is coincident with the western boundary of the Kaapvaal craton (Walraven et al. 1990; Sumner 1995) (Fig. 1).

Metamorphic overprint did not reach temperatures above 200 °C (Button 1973; Miyano and Beukes 1984). Most outcrops present sub-greenschist facies metamorphism, but amphibole is locally present due to Bushveld contact in the Malmani Subgroup, and supergene alteration during late fluid flow produced local Pb-Zn, fluorite, and gold deposits in both the Malmani and Cambellrand subgroups (Sumner and Beukes 2006).

The thickness of the Campbellrand Subgroup carbonates is about 1.5–2 km, with predominantly shallow-water subtidal to peritidal facies in the north and east. Platform slope and basinal deposits are preserved in the south and west (Fig. 1) and are about 500 m thick (Beukes 1980, 1987; Sumner 1997a, b). Shallow-water lithofacies include fenestrate microbialites, laminated planar, domal and columnar stromatolites, peloidal packstone to grainstone, and primary radial-fibrous precipitate, i.e. the so-called herringbone calcite (Sumner and Grotzinger 1996, 2000, 2004). Altermann and Schopf (1995) reported also about filamentous and colonial coccoid microbial fossil assemblage from drill core samples of stromatolite cherty limestones obtained at the Lime Acres.

Materials and methods

Sampling and lithofacies description

This research activity was carried out on eight main samples (2P1, 2P2, 2P3, 2P4; 4P1, 4P2, 4P3, 4S) from three different benches (2P, 4P and 4S) of the mine (Fig. 2). The preliminary lithofacies inspection was performed on prismatic chunks cut with a diamond wire (Fig. 3). Subsequently, chemical (X-ray fluorescence spectroscopy and C-S elemental analysis), mineralogical (X-ray diffraction with quantitative phase analysis), petrographic (optical polarizing and cold cathodoluminescence microscopy), and thermal (thermogravimetric and differential thermogravimetric analysis) analyses of the limestone, were coupled with burnability and technical tests on derived burnt lime samples.

Petrographic and cathodoluminescence analyses (optical polarizing microscopy)

The petrographic analysis was performed on 30 thin sections using an optical polarizing microscope (OPM) equipped with a high-resolution digital camera. Carbonate depositional textures were described according to the classification of carbonate rocks proposed by Dunham (1962), Friedman (1965), Embry and Klovan (1971), Sibley and Gregg (1987) (Table 2 and Fig. 4). Micrite refers to microcrystalline calcite crystals with size < 4 μm; microsparite indicates calcite crystals between 10 and 50 μm; sparite indicates clear calcite crystals larger than 62 μm (cf. Tucker and Wright 1990; Flügel 2004). Thin sections have also been examined under a cold cathodoluminescence microscope (CLM) performed with a Nuclide Luminoscope ELM 2B, operating at 10 kV with a beam current between 4 and 6 mA and vacuum gauge 60–80 mTorr, at the University of Milan.

Chemical analysis (X-ray fluorescence spectroscopy and C-S elemental analysis)

The terms of pure limestone, slightly dolomitic limestone, dolomitic limestone, calcitic dolomite, slightly calcitic dolomite and dolomite are used according to the chemical classification of carbonate rocks proposed by Frolova (1959), as reported in Chilingar (1960). The chemical analysis was carried out at ACME Analytical Laboratories
Ltd., Vancouver, Canada, either on limestone whole-rock

Fig. 2 **a** Stratigraphic log of the Ouplass Mine, Daniëlskuil, Griqualand West, South Africa with location of the analyzed samples. b Different landscapes of the mine with line drawing of stratigraphy. Five vertically superimposed benches are recognized, namely 2P, 3P, 4Pa, 4Pb, and 4S. Only benches 2P and 4P feed to stockpiles for the production of lime. Bench 3P is mined but rejected, probably because mainly dolomitic in composition. The top bench 4S is strongly silicicfied and belongs to the "cherty zone", which goes to optical sorting plant and is partially recovered for feeding to the stockpile.

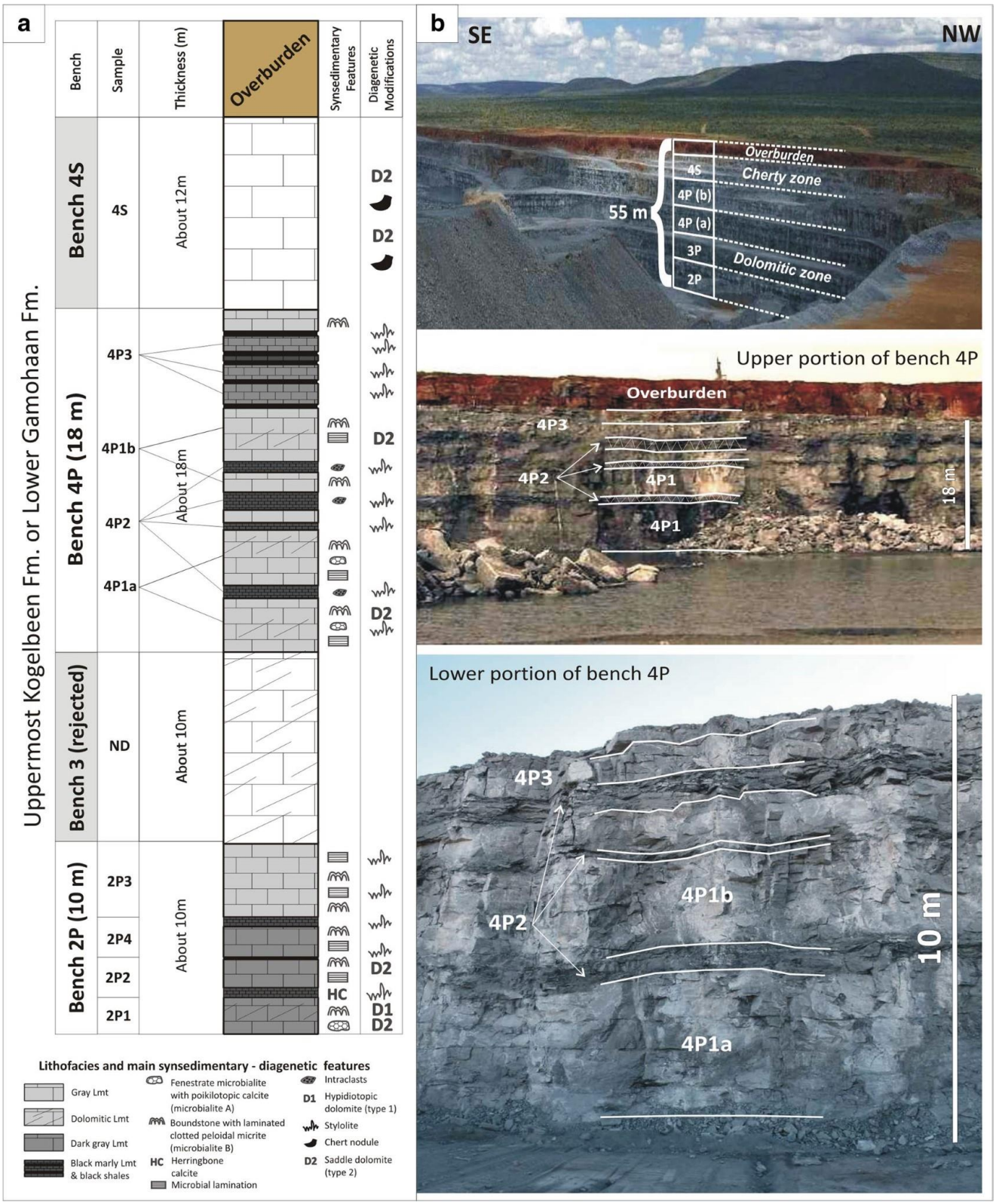

The overburden of this deposit is brownish colored

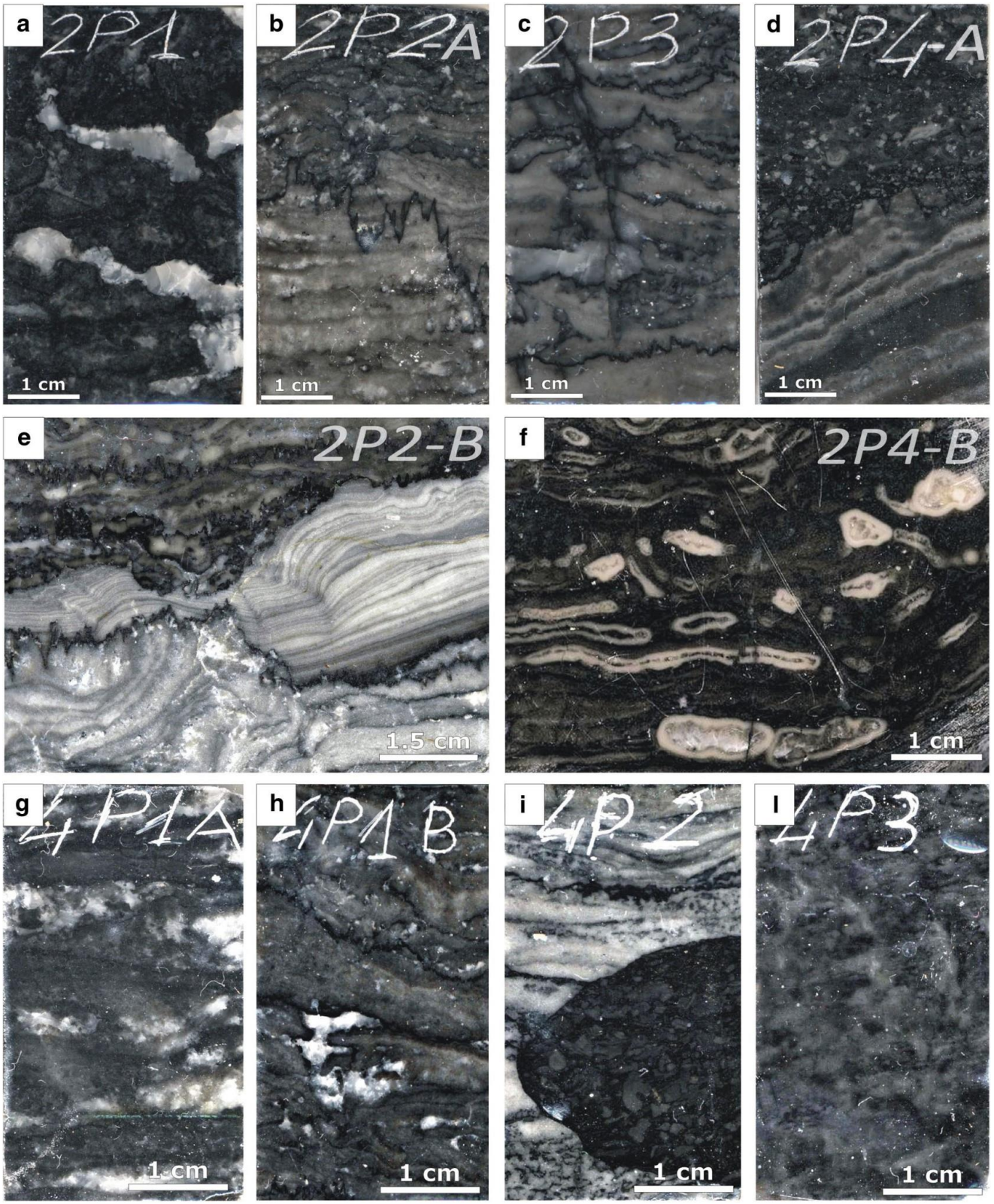

samples used for petrographic thin section preparation, ignition (LOI), afterward they were fused in a platinumor on lime samples burnt at 1050 and 1150 °C (Tables 3, gold crucible with lithium tetraborate flux. The molten 4, and 5). Samples were roasted to determine the loss on material was cast in a platinum mold, and fused discs

◂**Fig. 3** Lithofacies inspection of limestone samples from benches 2P and 4P of the Ouplaas Mine. **a** Dark gray microbial boundstone with irregular fenestrae (microbialite A) filled by coarse poikilotopic calcite cement (sample 2P1). **b** Laminated microbial boundstone made of micrite laminae recrystallized in microsparite (microbialite B) crossed by stylolites infilled by organic matter (sample 2P2). **c** Microbialite B with deformed recrystallized lamination crossed by black stylolites (sample 2P3). **d** Gray microbial boundstone (microbialite B) with peloidal intraclastic packstone/grainstone (sample 2P4). **e** Laminated microbial boundstone made of micrite laminae recrystallized in microsparite (microbialite B) crossed by stylolites (sample 2P2b). **f** Laminated microbial limestone with primary fenestral cavities with a first generation of isopachous fibrous marine cement and then coarse equant calcite (sample 2P4b). **g–h** Gray laminated microbial boundstone with irregular fenestrae filled by cement and black stylolites infilled by organic carbon (sample 4P1a-b). **i** Laminated microbialite with rounded mm-size intraclast (sample 4P2). **l** Packstone/grainstone with peloids and intraclasts (sample 4P3) were analyzed by a PANalytical Axios wavelength-dispersive X-ray fluorescence spectrometer (XRF-WDS). The declared detection limit was 0.01% for the major elements (SiO_2, Al_2O_3, Fe_2O_3, CaO, MgO, Na_2O, K_2O, MnO, TiO_2, P_2O_5, Cr_2O_3, Ba), while the detection limit was 0.002%, for SO_3, Sr, V_2O_5, and Zr, and was 0.001% for Cu, Ni, Pb, Zn. The analytical determination of total carbon (TC), total organic carbon (TOC), and total sulfur (S) was carried out by means of combustion infrared detection technique using a Leco CS844ES analyzer with detection limit 0.02%.

Diffraction analysis (X‑ray diffraction with quantitative phase analysis)

The X-ray powder diffraction analysis (XRD) was performed at the University of Milan-Bicocca using a Bragg–Brentano PANalytical X'Pert Pro PW3040/60 X-Ray diffractometer with CuKα radiation (1.5417 Å, 40 kV and 40 mA), over the angular 2θ-range 5–80°, with a divergence slit of 1/2° as instrumental setting with a counting time of 30 s/step and with a 0.02° step, on the same powdered samples used for the XRF and C-S elemental analyses. Samples were back-loaded on a flat sample-holder. The identification of mineral phases was performed running the PANalytical X'Pert High-Score software. The quantitative phase analysis (QPA) was performed running the GSAS-EXPGUI software package (Larson and Von Dreele 1994; Toby 2001) for the Rietveld refinement (Bish and Howard 1988; Young 1993) (Tables 6, 7, 8 and Fig. 5). The reliability of QPA has been checked comparing the chemical analysis of each sample determined by XRF with that calculated by theoretical chemical composition from the literature and the QPA determinations. Differences of these complementary chemical compositions are close, attesting the good accuracy of the QPA by XRD (Table 7).

Scanning electron microscopy

The microstructural analysis combined with the elemental analysis on whole-rock centimeter-sized limestone and burnt lime samples, polished and carbon coated, was performed at the University of Milan-Bicocca, using a Tescan Scanning Electron Microscope (SEM) equipped with an X-ray Dispersive Energy (EDX) spectrometer for microanalysis. The analysis was performed running high-vacuum mode for high-resolution backscattered electrons (BSE) and Secondary Electron (SE) imaging (Fig. 6).

Thermal analysis (thermogravimetric and differential thermogravimetric analysis)

Whole-rock centimeter-sized prismatic samples were fired in a Nabertherm thermogravimetric electric muffle furnace under air for 5 h (h). The thermal analysis (TG) was carried out adopting the following experimental conditions: preheating time of 2 h (h) for reaching the maximum temperature of 1200 °C, meaning a heating rate of about 10 °C/min, followed by 3 h of burning time at the maximum temperature. The obtained differential thermogravimetric (DTG) curves present typical intensive endothermal reaction peaks occurring for the thermal decomposition of carbonate phases in the temperature range between 600 and 1200 °C, but mostly at temperature > 700 °C (Emmerich 2011). Calcination parameters, i.e. starting and ending time, maximum peak and delta reaction time (t_1, t_2, t_{max}, Δt), starting and ending temperature, maximum peak and delta reaction temperature

(T_1, T_2, T_{max}, ΔT), were extrapolated from the TG-DTG analysis too (Table 9 and Fig. 7).

Burning and technical tests

Burning tests were carried out on whole-rock samples in a muffle furnace in air condition at different temperatures, 1050 and 1150 °C, adopting the following heating steps: preheating time of 2.5 h for reaching the maximum temperature, followed by 3 h of burning time at the maximum temperature. Subsequently, lime pebbles were crushed and then powdered into a ring mill. The residual CO_2 content and the reactivity of burnt limes were carried out according to the European calcimetry and slaking test methods (EN 459-2 2010). The procedure for testing the reactivity consists in measuring the temperature rise of a milk of lime obtained adding 150 g of powdered quicklime at time zero into a Dewar thermos containing 600 ml of water at 20 °C. The water with lime is kept in movement by an agitator at the speed of 400 rpm. The temperature rise (ΔT 40 °C or t_{60}), the maximum slaking temperature (T_{max}), and the Total Active Slaking Time (TAST) are determined. According to the European practice used throughout the lime producers,

Table 2 Results of petrographic analysis of limestone samples from bench 2P, 4P and 4S

Sample name	Lithofacies	Components	Diagenetic features	Cathodoluminescence (CLM)
2P[1]	Dark gray, slightly dolomitic fenestrate microbial boundstone (Fig. 3a) made of clotted peloidal micrite and microsparite crusts supporting fenestrate porosity filled by calcite (microbialite A)	Cm-sized sub-rounded fenestral voids filled by herringbone calcite and equant to poikilotopic calcite cement (Fig. 4a–b). Dark kerogen soaks microsparite rims	Herringbone calcite: cloudy radial fibrous banded calcite fans represent the primary marine cement associated with dark microbial laminae. Fenestrate porosity, locally enlarged by dissolution, is filled by equant drusy mosaic and cm-size poikilotopic calcite cement (burial diagenesis). Dolomite (Fig. 4a) up to %. Dolomite type 1: hypidiotopic mosaic of subhedral dolomite crystals µm) mimetic to replacive on clotted peloidal micrite (early diagenetic). Dolomite type 2: cloudy rhombohedral crystals (200–500 µm) of saddle dolomite with undulose extinction and etched crystal rims replacive on poikilotopic calcite (burial diagenesis). Stylolites and solution seams due to pressure solution	The clotted peloidal micrite/microsparite crusts locally present primary nonluminescent microbial microstructures (dark peloids and filaments). The equant and the poikilotopic calcites are orange dull, rarely zoned and contain small, nonluminescent crystals of dolomite. The first generation of kerogen soaking the fenestral porosity is opaque under CLM, while subsequent generations are orange bright in the CLM observations same conditions
2P[2]	Gray, slightly dolomitic microbial boundstone (Fig. 3b–e) with mm- thick clotted peloidal micrite/microsparite laminae microbialite B) and herringbone calcite passing into clotted peloidal packstone/grainstone with subordinate fenestrate microbialite A	Alternation of dark gray micrite/microsparite laminae and light fibrous radial calcite laminae (herringbone calcite) and inferred originally aragonitic botryoidal fans. Matrix of micritetomicrosparite with peloidal remnants. Microsparite and sparite range in size from 20 microns to 200 µm but mean size is –100 µm. Fenestrae with equant or poikilotopic calcite and impregnated by different films of opaque organic carbon Fig. 4c)	Neomorphic microsparite and sparite due to recrystallization of micrite. Fabric-replacive hypidiotopic dolomite (type 1). Sub mm-sized rhombohedral dolomite crystals (type 2) post date them m-size poikilotopic calcite cement in horizontal voids. Stylolites with organic carbon kerogen) are often associated with partial dolomitization and recrystallization. Few scattered low to high amplitude blackstylolites associated with brownish type 2 saddle dolomite	Equant and poikilotopic calcite are orange with a few dull/bright zonation and a late, thin yellow growth phase. Nonluminescent dolomite crystals are locally crossed by black stylolites. The first thin film of kerogen is generally nonluminescent conversely, subsequent layers are orange bright luminescent under the same optical conditions
2P[3]	Gray laminated microbial boundstone microbialite B; Fig. 3c) with subordinate fenestrate microbialite A, associated with marl sand black shales. Locally coated grain and peloidal packstone/grainstone	Micrite and neomorphic microsparite micrite. Cloudy radial fibrous banded calcite fans (herringbone calcite). Cavities filled by equant and poikilotopic calcite (100–200 µm) (Fig. 4d)	Neomorphic microsparite and sparite due to recrystallization of micrite. A few tensional fractures with equant and poikilotopic calcite are cut by late stylolites	Clotted pelodal micritetomicrosparite microbial laminae present well recognizable, nonluminescent small peloids. Equant calcite in small cavities is orange and poorly zoned
2P[4]	Gray microbial boundstone (microbialite B) with tubular cavity framework with subordinate fenestrate microbialite A and peloidal intraclastic packstone/grainstone (Fig. 3d–f)	Tubular structures (possible microfossils; Fig. 4g). Cavity filling is represented by a thin dark micrite rim, not recrystallized, and then by two calcite cements: the first fibrous radial, the second equant calcite, often post dated by poikilotopic calcite	Recrystallization of the microbial micrite into microsparite to sparite. Cavities are filled by kerogen, which soaked along stylolites after the pressure solution. Different cement generations, possibly related to late diagenetic fluids. Frequent fluid inclusions (along twinning) in the poikilotopic calcite	In the clotted peloidal microsparite peloids are recognizable because nonluminescent. A few poikilotopic calcite crystals present preserved microbial microstructures

)

Table2 continued

Samplename	Lithofacies	Components	Diageneticfeatures	Cathodoluminescence(CLM)
$_4P^1$ (	Graylaminatedmicrobialboundstone microbialiteB;Fig. 3g–h)passinginto peloidalpackstone/grainstonewithsub-ordinatefenestratemicrobialiteA	Clottedpeloidalmicritelaminaeand fenestralvoidsfilledbycement	Neomorphicmicrospariteoverclotted peloidalmicrite.Largefenestraefilled byequantandpoikilotopiccalcite.Fre-quentlatediageneticstylolitescutallthe otherdiageneticfeatures	Theequantandpoikilotopiccalcitesare orangedull,rarelyzonedandcontain small,non-luminescentcrystalsof dolomite.Clottedpeloidalmicrosparite presentswell-preserved,non-luminescent smallpeloids
$_4P^2$	Graydolomiticmarlymicrobialbound-stone(microbialiteB)formingsphe-roidalordomalstromatoliteswithdark lamination,whitebands(herringbone calcite),andcm-sizeintraclastsof peloidalgrainstone(Figs. 3iand 4e–f), associatedwithblackshales(Fig. 2)	Cm-sizednodulescomposedofsub-sphericalgrainsofrecrystallizeddark graypeloidalandmicrobialmicrite. Cloudyradialfibrousbandedcalcitefans herringbonecalcite	Radialfibrousherringbonecalciteand therecrystallizedneomorphiccoarse sparite.Coarsesparitepostdatesstylo-lites.Abundantlowtomediumampli-tudeblackkerogenandpyrite-enriched stylolitesandsolutionseamsinshales	Patchesofwell-preservedpeloidalclot-tedmicriteassociatedwithequantand poikilotopiccalcite.Manystyloliteswith blacknon-luminescentopaqueminerals andkerogen(orangeluminescent)(Fig. 4 e–f)
$_4P^3$	Darkgraytoblacklaminatedmudstone(wackestonetopackstone/grainstone withpeloids,intraclastsandareasof microbialboundstone(microbialiteB; Fig. 3l)	Lackofpoikilotopiccalcite.Peloidal packstone/grainstoneassociatedwith neomorphicsparite	Clottedpeloidalmicriteandmicrosparite Fig. 4g)withintergranularcementa-(tion,smallprimaryfenestralcavities.No solutionseamsandstylolites	Morehomogenousclottedpeloidalorange luminescentmicrosparitewithpreserved non-luminescentpeloids.Smallprimary intergranularcavitiesfilledbyorange, poorlyzonedequantcalcite
$_4S$	Chertylimestone(Figs. 2and 4h)made ofcoarsesparitewithmicrocrystalline quartzandsuperimposedrhombohedral dolomite	Chertandneomorphicspariteover probablyclottedpeloidalmicriteand microsparite	Chertreplacementoncoarseneomorphic sparite.Dolomite(type2,saddledolo-miteduringburialdiagenesis)postdates silicification	

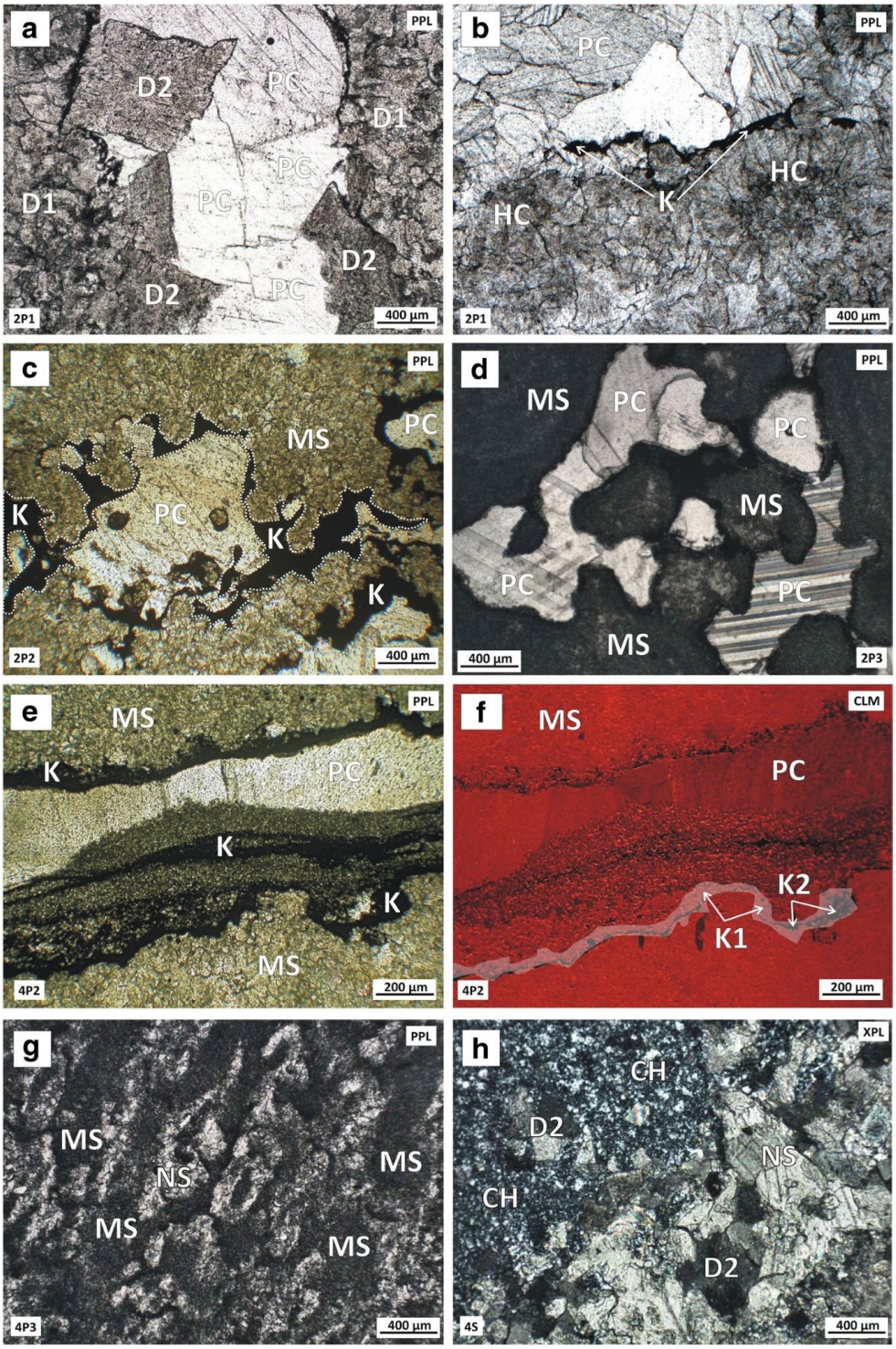

Fig. 4 Petrographic and cathodoluminescence analysis of limestone samples from benches 2P, 4P and 4S of the Ouplaas Mine. **a** Fenestrate microbialite (microbialite A) with centimeter-size fenestral voids filled by clear and twinned poikilotopic calcite associated with type 1 hypidiotopic dolomite (D1) and late burial brownish type saddle dolomite (D2) (sample 2P1). **b** Cloudy radial fibrous marine precipitate, i.e. herringbone calcite (sample 2P1). **c** Laminated clotted peloidal micrite (microbialite B) cut by stylolites enriched by kerogen (sample 2P2). **d** Fenestrate microbilite with poikolotopic calcite and clotted peloidal micrite (microbialite B) (sample 2P3). **e-f** Enlarged cavity with different layers of microsparite, thin layers of black carbon (kerogen) associated with stylolites, and poikilotopic calcite (sample 4P2). Kerogen segregation on the rims (sample 4P2). **g** Laminated clotted peloidal micrite and microsparite (sample 4P3). **h** Chert replacement on coarse sparite is superimposed by burial saddle dolomite (sample 4S). Symbols legend: PPL: plane polarized light; XPL: crossed polarized light; CLM: cathodoluminescence microscopy. Main diagenetic features: EQ: equant calcite, HC: herringbone calcite. D1:

hypidiotopic mimetic or fabric-replacive dolomite (type 1), SS: stylolites and solution seams, K: carbon black (kerogen) segregation, K1: kerogen bright luminescent under CLM, K2: kerogen non-luminescent under CLM, MS: microsparite, PC: poikilotopic calcite, NS: neomorphic coarse sparite, CH: chert replacement, D2: saddle brownish dolomite replacement (type 2)

when t_{60} < 3 min. the reactivity is high (t_{60} < 1 min. very high), when t_{60} is between 3 and 6 min. the reactivity is medium, and when t_{60} > 6 min. the reactivity is low. The available lime index (ALI) was determined according to the sugar method (ASTM C25 2011), where a definite portion of quicklime is dissolved in a sugar solution and titrated against standardized HCl solution (Tables 10, 11, 12, 13 and Fig. 8).

Results

Limestone characterization

Five main carbonate lithofacies have been distinguished and summarized in Table 2:

Table 3 Results of chemical analysis (XRF-WDS and C-S elemental analysis) of limestone samples from the quarry

Code	LLD	2P1	2P2	2P3	2P4a	2P4b	2P4c	2P4d	4P1a	4P1b	4P2a	4P2bs	4P3
Class		SDL	L	L	L	L	SDML	SDL	L	L	ML	BS	L
LOI	0.01	43.48	43.7	43.55	43.58	43.32	42.98	43.32	43.67	43.66	42.39	26.46	43.56
SiO_2	0.01	0.91	0.15	0.43	0.18	0.63	2.04	1.04	0.05	0.09	1.99	29.64	0.02
Al2O3	0.01	0.06	0.02	0.11	< 0.01	0.06	0.09	0.07	< 0.01	< 0.01	0.59	11.51	< 0.01
Fe2O3	0.01	0.16	0.11	0.1	0.07	0.08	0.15	0.14	0.1	0.09	0.29	2.31	0.07
CaO	0.01	53.09	54.53	54.94	55.33	54.85	53.1	54.43	54.87	54.84	53.58	20.28	55.54
MgO	0.01	1.59	0.92	0.44	0.19	0.34	1.23	1.13	0.33	0.38	0.4	1.99	0.17
Na_2O	0.01	< 0.01	< 0.01	< 0.01	< 0.01	< 0.01	< 0.01	< 0.01	< 0.01	< 0.01	< 0.01	0.08	< 0.01
K_2O	0.01	< 0.01	< 0.01	0.02	< 0.01	0.01	0.01	< 0.01	< 0.01	< 0.01	0.17	4.02	< 0.01
MnO	0.01	0.62	0.67	0.79	0.63	0.62	0.6	0.66	0.71	0.66	0.62	0.14	0.5
SO_3	0.002	0.057	0.004	0.044	0.006	0.008	0.029	0.019	0.009	0.012	0.368	2.892	0.019
TiO_2	0.01	0.01	< 0.01	0.01	< 0.01	0.01	< 0.01	0.02	< 0.01	0.01	0.03	0.55	< 0.01
P2O5	0.01	< 0.01	< 0.01	< 0.01	< 0.01	< 0.01	< 0.01	< 0.01	< 0.01	< 0.01	< 0.01	0.05	< 0.01
Cr2O3	0.01	< 0.01	< 0.01	< 0.01	< 0.01	< 0.01	< 0.01	< 0.01	< 0.01	< 0.01	< 0.01	0.02	< 0.01
Ba	0.01	< 0.01	< 0.01	< 0.01	< 0.01	< 0.01	< 0.01	< 0.01	< 0.01	< 0.01	< 0.01	< 0,01	< 0.01
Cu	0.001	< 0.001	< 0.001	< 0.001	< 0.001	< 0.001	< 0.001	0.002	< 0.001	< 0.001	0.002	0.005	< 0.001
Ni	0.001	< 0.001	0.002	< 0.001	< 0.001	< 0.001	< 0.001	< 0.001	< 0.001	< 0.001	< 0.001	0.006	< 0.001
Pb	0.001	0.003	0.002	< 0.001	0.004	< 0.001	0.002	0.002	0.002	0.002	0.002	0.004	0.002
Sr	0.002	< 0.002	0.003	0.002	< 0.002	0.002	0.003	0.003	0.003	0.003	0.003	0.002	< 0.002
V2O5	0.002	< 0.002	0.003	0.002	< 0.002	< 0.002	0.003	< 0.002	< 0.002	< 0.002	< 0.002	0.016	< 0.002
Zn	0.001	< 0.001	< 0.001	< 0.001	< 0.001	< 0.001	< 0.001	< 0.001	< 0.001	< 0.001	< 0.001	0.001	< 0.001
Zr	0.002	< 0.002	< 0.002	< 0.002	< 0.002	< 0.002	< 0.002	< 0.002	< 0.002	< 0.002	< 0.002	0.008	< 0.002
SUM	–	100.0	100.1	100.4	100.0	99.9	100.2	100.8	99.7	99.7	100.4	99.9	99.9
TOT/C	0.02	12.51	12.43	12.41	12.33	12.75	12.28	12.48	12.81	12.46	12.54	14.26	12.64
TOT/S	0.02	0.03	< 0.02	< 0.02	< 0.02	< 0.02	< 0.02	< 0.02	< 0.02	< 0.02	0.2	1.68	< 0.02
C/ORG	0.02	0.59	0.75	0.75	0.64	1.27	1.26	1.0	1.17	1.02	1.33	1.13	0.89
CaO/MgO	–	33.4	59.3	124.9	291.2	161.3	43.2	48.2	166.3	144.3	134.0	10.19	326.7
H.I	–	1.6	0.9	0.5	0.2	0.4	1.3	1.2	0.3	0.4	0.5	Nd	0.2

The carbonate classification is based on Frolova (1959) that considers the CaO/MgO ratio criterion

Symbols legend: *SDL* slightly dolomitic limestone, *L* pure limestone, *SDML* slightly dolomitic marly limestone, *ML* marly limestone, *BS* black shale, *TOT/C* total carbon, *TOT/S* total sulfur, *C/ORG* organic carbon, *H.I*. hydraulic index according to Elsen et al. (2011)

Code	LLD	2P1	2P2	2P3	2P4	4P1b	4P2a	4P2b	4P3
SiO_2	0.01	1.22	0.25	2.4	1.4	0.17	1.69	2.21	0.07
Al2O3	0.01	0.10	0.03	0.8	< 0.01	0.03	0.43	0.66	0.03
Fe2O3	0.01	0.40	0.19	0.3	0.2	0.15	1.17	1.89	0.14
CaO	0.01	93.11	96.88	93.6	96.0	98.35	89.36	81.91	99.75
MgO	0.01	4.43	1.43	1.1	1.2	0.61	6.02	11.46	0.29
Na_2O	0.01	< 0.01	0.01	< 0.01	< 0.01	< 0.01	< 0.01	< 0.01	< 0.01
K_2O	0.01	0.01	< 0.01	0.2	< 0.01	< 0.01	0.08	0.15	< 0.01
MnO	0.01	1.16	1.17	1.4	1.1	1.19	1.36	1.54	1.08
TiO_2	0.01	0.01	0.02	< 0.01	< 0.01	0.01	0.03	0.04	0.01
SO_3	0.002	0.10	0.02	0.3	0.1	0.16	0.44	0.33	0.01

Sr	0.002	< 0.01	0.01	< 0.01	< 0.01	0.01	0.01	< 0.01	< 0.01
SUM	–	100.5	100.0	100.2	100.0	100.7	100.6	100.2	101.4
TOT/C	0.02	0.19	0.21	0.15	0.26	0.19	0.2	0.14	0.21
TOT/S	0.02	0.07	0.03	0.12	0.03	0.02	0.11	0.1	0.02

Table 4 Results of chemical analysis (XRF-WDS and C-S elemental analysis) on burnt lime samples at 1050 °C (normalized)

Code	LLD	2P1a	2P1b	2P2	2P3	2P4	4P1b	4P2a	4P2b	4P3a	4P3b
SiO_2	0.01	0.61	1.39	0.17	2.06	1.18	0.04	1.51	2.21	0.07	0.10
Al2O3	0.01	0.06	0.07	0.02	0.65	0.02	< 0.01	0.43	0.90	0.04	0.05
Fe2O3	0.01	0.24	0.34	0.13	0.30	0.13	0.18	0.72	1.66	0.17	0.17
CaO	0.01	95.9	94.7	98.3	94.5	97.6	98.1	92.7	82.7	98.0	98.5
MgO	0.01	2.52	2.84	0.79	1.08	0.40	0.54	3.19	10.52	0.36	0.32
Na_2O	0.01	< 0.01	< 0.01	< 0.01	0.01	< 0.01	< 0.01	0.07	< 0.01	< 0.01	< 0.01
K_2O	0.01	< 0.01	< 0.01	< 0.01	0.14	< 0.01	< 0.01	0.08	0.20	< 0.01	< 0.01
MnO	0.01	1.09	1.09	1.17	1.42	1.13	1.18	1.26	1.41	1.02	0.92
TiO_2	0.01	0.01	0.02	< 0.01	0.03	0.02	0.02	0.02	0.06	< 0.01	0.03
SO_3	0.002	0.04	0.14	< 0.01	0.08	0.01	0.09	0.29	0.41	0.08	0.07
Sr	0.002	< 0.01	< 0.01	< 0.01	< 0.01	< 0.01	< 0.01	< 0.01	< 0.01	< 0.01	< 0.01
SUM	–	100.5	100.6	100.5	100.3	100.5	100.2	100.3	100.1	99.7	100.2
TOT/C	0.02	0.19	0.16	0.12	0.12	0.13	0.1	0.14	0.1	0.1	0.12
TOT/S	0.02	0.03	0.04	< 0.02	0.03	< 0.02	< 0.02	0.09	0.14	0.04	0.03

Table 5 Results of chemical analysis (XRF-WDS and C-S elemental analysis) on burnt lime samples at 1150 °C (normalized)

Code	2P1	2P2	2P3	2P4a	2P4b	2P4c	2P4d	4P1a	4P1b	4P2a	4P2bs	4P3
Rwp	9.07	9.22	9.38	8.92	9.10	9.21	9.04	8.88	8.83	9.52	12.84	8.95
χ2	3.84	3.77	4.45	4.11	3.98	3.83	3.92	3.68	3.72	4.37	5.38	4.05
Cal	92.8	95.8	97.9	99.8	98.4	93.1	94.6	99.1	99.1	95.2	37.1	99.7
Dol	6.6	4.0	1.8	0.2	1.2	5.1	4.6	0.9	0.9	1.3	2.0	0.3
Qtz	0.6	0.2	0.3	0.0	0.4	1.7	0.8	0.0	0.0	1.2	4.8	
Ill										1.6	48.5	
Chl											3.2	
Py										0.7	1.8	
Pl									Tr		2.4	

Table 6 Results of X-Ray diffraction quantitative phase analysis (XRD-QPA) of limestone samples

Agreement factors (R_{wp}, χ^2) for the Rietveld refinement (Larson and Von Dreele 1994). Symbols legend: fundamental mineral phases, Cal: Calcite: α-$CaCO_3$; Dol: Dolomite: $CaMg(CO_3)_2$; Qtz: Quartz: α-SiO_2;

Subordinated mineral phases: Ill: Illite $^{+2}$, Fe $^{+3})_6AlSi_3O_{10}(OH)(\ _8H$; Py: Pyrite: α-$FeS_3O$, K)y$(Al_4{\cdot}Fe_4{\cdot}Mg_2$; Pl: plagioclase $(Na,Ca)(Si,Al)_4{\cdot}Mg_6)(Si_{8\text{-}y}{\cdot}Al_y)O_{20}(OH)_4$; Chlorite: Chl: $_4O_8$

Chlorite (Mg, Fe

Abbreviations of minerals according to Whitney and Evans (2010)

1) dark gray fenestrate microbial boundstone, slightly dolomitic with fibrous herringbone calcite (microbialite A, sample 2P1; Figs. 3a and 4a–b),

2) gray microbial boundstone, slightly dolomitic (samples 2P2, 2P4, and 4P1), with laminated clotted peloidal micrite (microbialite B), sometimes associated with tubular cavity framework (2P4) and subordinated fenestrate microbialite A (Figs. 3b, d–h and 4c),
3) gray marly limestone associated with sporadic black shales made of dolomitic microbial boundstone (microbialite B) with coated grains and characterized by abundant stylolites and solution seams with kerogen and pyrite (samples 2P3 and 4P2; Figs. 3c, i and 4d–f),
4) dark gray pure limestone (sample 4P3; Figs. 3l and 4g) with centimeter-sized beds of intraclastic packstone to grainstone, peloidal mudstone-wackestone, locally passing into boundstone with laminated clotted peloidal micrite (microbialite B).
5) dark gray cherty limestone (sample 4S; Fig. 4h) with black nodules of replacive chert on coarse neomorphic sparite. This last lithofacies goes to the optical sorting plant and is partially recovered for feeding to the stockpile.

Table 7 Results of bulk chemical composition of limestone samples determined by XRF and calculated by XRD

Code	2P1			2P2			2P3			2P4a			2P4b			2P4c			2P4d			4P1a			4P1b			4P2a			4P2b			4P3		
Det	XRD	XRF	Δ	XRD	XRF	Δ	XRD	XRF	Δ	XRD	XRF	Δ	XRD	XRF	Δ	XRD	XRF	Δ	XRD	XRF	Δ	XRD	XRF	Δ	XRD	XRF	Δ	XRD	XRF	Δ	XRD	XRF	Δ	XRD	XRF	Δ
SiO_2	0.6	0.9	−0.3	0.2	0.2	0.1	0.3	0.4	−0.1	0.0	0.2	−0.2	0.4	0.6	−0.2	1.7	2.0	−0.3	0.8	1.0	−0.2	0.0	0.1	−0.1	0.0	0.1	−0.1	2.1	2.0	0.1	33.5	29.6	3.9	0.0	0.0	0.0
Al_2O_3	0.0	0.1	−0.1	0.0	0.0	0.0	0.0	0.1	−0.1	0.0	<0.01	–	0.0	0.1	−0.1	0.0	0.1	−0.1	0.0	0.1	−0.1	0.0	<0.01		0.0	<0.01		0.3	0.6	−0.3	9.2	11.5	−2.3	0.0	<0.01	
Fe_2O_3	0.0	0.2	−0.2	0.0	0.1	−0.1	0.0	0.1	−0.1	0.0	0.1	−0.1	0.0	0.1	−0.1	0.0	0.2	−0.2	0.0	0.1	−0.1	0.0	0.1	−0.1	0.0	0.1	−0.1	0.3	0.3	0.0	2.1	2.3	−0.2	0.0	0.1	−0.1
CaO	54.0	53.1	0.9	54.9	54.5	0.4	55.4	54.9	0.5	56.0	55.3	0.6	55.5	54.9	0.6	53.8	53.1	0.7	54.4	54.4	0.0	55.8	54.9	0.9	55.8	54.8	1.0	53.7	53.6	0.2	21.5	20.3	1.3	56.0	55.5	0.4
MgO	1.4	1.6	−0.1	0.9	0.9	−0.1	0.4	0.4	0.0	0.0	0.2	−0.1	0.3	0.3	−0.1	1.1	1.2	−0.1	1.0	1.1	−0.1	0.2	0.3	−0.1	0.2	0.4	−0.2	0.3	0.4	−0.1	2.8	2.0	0.8	0.1	0.2	−0.1
Na_2O	0.0	<0.01	–	0.0	<0.01	–	0.0	<0.01	–	0.0	<0.01	–	0.0	<0.01	–	0.0	<0.01	–	0.0	<0.01	–	0.0	<0.01	–	0.0	<0.01		0.0	<0.01	–	0.1	0.1	0.1	0.0	<0.01	–
K_2O	0.0	<0.01	–	0.0	<0.01	–	0.0	0.0	0.0	0.0	<0.01	–	0.0	0.0	0.0	0.0	0.0	0.0	0.0	<0.01	–	0.0	<0.01	–	0.0	<0.01		0.1	0.2	−0.1	3.5	4.0	−0.5	0.0	<0.01	–
MnO	0.0	0.6	−0.6	0.0	0.7	−0.7	0.0	0.8	−0.8	0.0	0.6	−0.6	0.0	0.6	−0.6	0.0	0.6	−0.6	0.0	0.7	−0.7	0.0	0.7	−0.7	0.0	0.7	−0.7	0.0	0.6	−0.6	0.0	0.1	−0.1	0.0	0.5	−0.5
SO_3	0.0	0.1	−0.1	0.0	0.0	0.0	0.0	0.0	0.0	0.0	0.0	0.0	0.0	0.0	0.0	0.0	0.0	0.0	0.0	0.0	0.0	0.0	0.0	0.0	0.0	0.0	0.0	0.5	0.4	0.1	1.2	2.9	−1.7	0.0	0.0	0.0
TiO_2	0.0	0.0	0.0	0.0	<0.01	–	0.0	0.0	0.0	0.0	<0.01	–	0.0	0.0	0.0	0.0	<0.01	–	0.0	0.0	0.0	0.0	<0.01		0.0	0.0	0.0	0.0	0.0	0.0	0.0	0.6	−0.6	0.0	<0.01	
LOI	44.0	43.5	0.5	44.0	43.7	0.3	43.9	43.6	0.4	44.0	43.6	0.4	43.8	43.3	0.5	43.4	43.0	0.4	43.8	43.3	0.5	44.0	43.7	0.3	44.0	43.7	0.3	42.8	42.4	0.4	25.8	26.5	−0.7	44.0	43.6	0.4

Differences of complementary chemical compositions (Δ) are close among them. Attesting the good accuracy of the quantitative phase analysis (QPA) by X-ray diffraction analysis (XRD)

These microfacies include various diagenetic features such as: radial fibrous banded cement, i.e. the herringbone calcite

(cf. Sumner and Grotzinger 1996, 2004), neomorphic microsparite after recrystallizion of micrite, equant drusy and poikilotopic sparite cements, mimetic or fabric-replacive hypidiotopic dolomite (type 1), stylolites and solution seams, organic carbon (kerogen) segregation and impregnation, chert, and saddle dolomite (type 2) (cf. Figs. 3, 4 and Table 2).

Chemical (XRF-WDS and C-S elemental analysis), and mineralogical (XRD-QPA) analyses attest the presence of subordinated non-carbonate impurity, which is mainly ascribed to clay and opaque minerals (Fig. 5, Tables 3 and 6). The silica content generally ranges between 0.02 up to 2.04%, but can reach the 30% in sporadic black shales associated with gray dolomitic limestones (cf. sample 4P2bs, Table 3). The calcite content generally varies between 92% up to 99% on the whole rock, but locally it can be lower, especially within the black shales where calcite is just the 37%. Sample 4P2 present the lowest content of carbonates and the highest content of impurity. Impurities are mainly represented by dolomite (2P1, 2P4), quartz (4P2, 2P3), clay minerals (4P2, 2P3) and pyrite (4P2, 2P4, 4P3), coupled with organic carbon (kerogen). Gray marly limestone samples, namely 2P3 and 4P2, locally present microcrystalline quartz and clay minerals, i.e. illite and chlorite, associated with pyrite and abundant organic carbon. These impurities are particularly concentrated along stylolites.

The SEM-EDX microanalysis confirms the chemical composition of clay minerals (Fig. 6). Moreover some chemical maps on different limestone samples pointed out the ubiquitous distribution of the manganese oxide, which is probably diffused as microcrystalline braunite within the fine matrix of the whole-rock, reaching the average content of 0.65%.

The thermal analysis (TG-DTG) points out some significant burnability differences between samples from different strata (Table 9 and Fig. 7). The plot A, showing the ignition loss (%) vs. time (s) (Fig. 7a), permits to extrapolate the calcination velocity (g/s), pointing out the highest velocity for sample 2P1, followed by sample 4P2. Plot B, showing the DTG normalized curve (Fig. 7b), points out the mass flow ((g/s)/$g_{initial}$%) as a function of burning temperature (°C). All samples present a single peak of dissociation because they are mainly calcitic in composition. The only exception is sample 4P2, which presents double peaks of dissociation, indicating the presence of a double carbonate, most likely dolomite (Gunasekaran and Anbalagan 2007). The first peak at lower temperature is due to the dissociation of the magnesium molecule ($MgCO_3$), with the formation of periclase and calcite, while the second peak at the highest temperature is due to the dissociation of the calcitic molecule ($CaCO_3$), according to the literature (Boynton 1980; Emmerich 2011). The height of the peaks is proportional to the total CO_2 emission. The weight loss (LOI) between 200 and 600 °C is due to the content of bound water of clay minerals and to the organic carbon (kerogen).

Table 8 Results of X-Ray diffraction quantitative phase analysis (XRD-QPA) of burnt lime samples at 1050 and 1150 °C

Code	2P1	2P2	2P3	2P4	4P1b	4P2a	4P2b	4P3	2P1a	2P1b	2P2	2P3	2P4	4P1	4P2a	4P2b	4P3a	4P3b
Burning T (°C)	1050	1050	1050	1050	1050	1050	1050	1050	1150	1150	1150	1150	1150	1150	1150	1150	1150	1150
R_{wp}	6.5	6.5	6.2	6.0	6.7	6.2	5.4	6.0	6.8	6.2	6.2	6.3	6.5	6.3	6.6	8.7	6.6	6.5
χ^2	3.3	3.0	3.0	2.8	2.4	3.4	2.9	2.8	3.4	3.0	2.9	3.0	3.0	3.0	3.5	5.8	3.4	3.1
Lime	88.5	91.9	88.6	92.6	94.8	83.0	74.6	94.8	92.5	88.8	95.0	89.7	92.2	95.4	88.2	76.3	95.5	94.9
Periclase	4.8	1.3	0.6	1.3	0.25	6.3	11.6	0.6	2.5	2.7	0.3	Tr	Tr	Tr	3.0	11.2	0.6	
Quartz	1.0			0.7		0.7	Tr			Tr								
Larnite			4.1	0.9		1.5	0.9	0.5		0.5		2.2	3.7		3.2	3.8	Tr	Tr
Hatrurite										0.8						1.9		
Merwinite		2.0	2.5	1.0		2.9	5.8			3.3		Tr			0.7	Tr		2.6
Tricalcium aluminate		0.9	Tr						0.7		0.5	1.6		Tr	Tr	Tr		
Gehlenite						Tr	Tr					1.7				Tr		
Srebrodolskite	Tr	Tr				1.3	2.9								2.3	4.4		
Dicalcium manganate	6.0	3.9	4.2	3.5	4.9	4.1	4.0	4.0	4.4	3.5	4.0	4.4	4.1	3.8	2.4	2.5	3.6	2.4
Fersilicide	Tr								Tr	Tr	Tr				Tr	Tr	Tr	Tr
Anhydrite	Tr	Tr	Tr			Tr	Tr		Tr		Tr			1.1		Tr		

Agreement factors (R_{wp}, χ^2) for the Rietveld refinement according to Larson and Von Dreele (1994). Legend of symbols: fundamental mineralogical phases: Lime = CaO; Periclase: MgO; subordinated mineral phases: Quartz: α-SiO_2; Larnite: Ca_2SiO_4; Hatrurite: Ca_3SiO_5; Merwinite: $Ca_3Mg(SiO_4)_2$; Tricalcium Aluminate: $Ca_3Al_2O_6$; Gehlenite: $Ca_2Al(AlSi)O_7$; Srebrodolskite: $Ca_2Fe^{3+}{}_2O_5$; Dicalcium Manganate: Ca_2MnO_4; Fersilicide: FeSi; Anhydrite: $CaSO_4$; Tr = traces (< 0.5%)

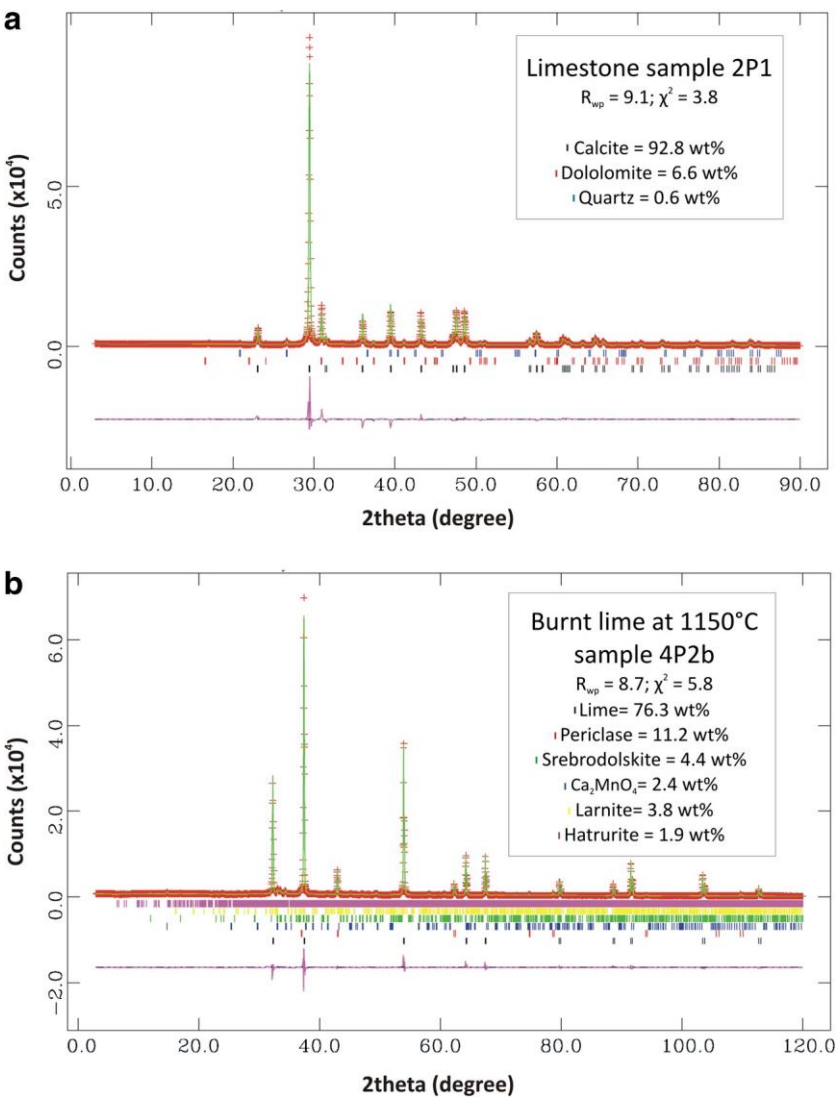

Fig. 5 Observed (crosses), calculated (continuous line) and difference (bottom line) profiles for Rietveld refinements of XRD powder patterns of **a** Limestone sample 2P1 in the angular range 3–90° 2θ, and **b** Lime sample 4P2 burnt at 1150 °C in the angular range 3–120° 2θ. Vertical bars mark Bragg peak positions

Burnt lime characterization

Burnt lime presents a typical brownish color, which is light brown at 1050 °C, pale brown at 1150 °C, and medium brown to dark gray at 1200 °C. The only exception is represented by very thin layers of siliciclastic impurity along stylolites, which are generally whitish after the thermal shock. Chemical (XRF-WDS and C-S elemental analysis) and mineralogical (XRD-QPA) analysis of burnt limes (Table 8) shows that lime (CaO) ranges from 75% up to 95%. The following subordinated mineral phases were identified: periclase (MgO – max 12%), dicalcium manganate ($Ca_2(MnO_4)$ – max 6%), larnite (Ca_2SiO_4 – max 4%), hatrurite (Ca_3SiO_5 – max 2%), quartz (SiO_2 – max 1%); merwinite ($Ca_3Mg(SiO_4)_2$ – max 6%); tricalcium aluminate ($Ca_3Al_2O_6$ – max 2%) and srebrodolskite ($(Ca_2Fe^{3+}{}_2O_5)$ – max 4%). Finally, some accessorial minerals (< 0.5%), were also determined: gehlenite ($Ca_2Al(AlSi)O_7$); fersilicide (FeSi) and anhydrite ($CaSO_4$).

The SEM-EDX analysis, performed on burnt chunk samples, confirms the composition of accessory mineral phases already detected by means of XRD analysis. It points out different calcium and magnesium silicate burnt products, mostly concentrated along stylolites. They appear with apparently fluidal textures, probably indicating a partially and very localized melting (Fig. 6b).

According to the slaking test method (EN 459-2 2010), the reactivity of lime burnt at 1050 °C is very high (t_{60} < 1 min.) for samples 2P1, 2P4 and 4P3, high (t_{60} < 2 min.) for samples 2P2, 2P3, 4P1 and medium (t_{60} = 4 min.) for sample 4P2. In any case, the average reactivity at 1050 °C is high (t_{60} = 1.3 min., T_{max} = 72.3 °C) (Table 10 and Fig. 8a). Conversely, burnt lime at 1150 °C generally presents a low reactivity. Especially, samples 2P2,

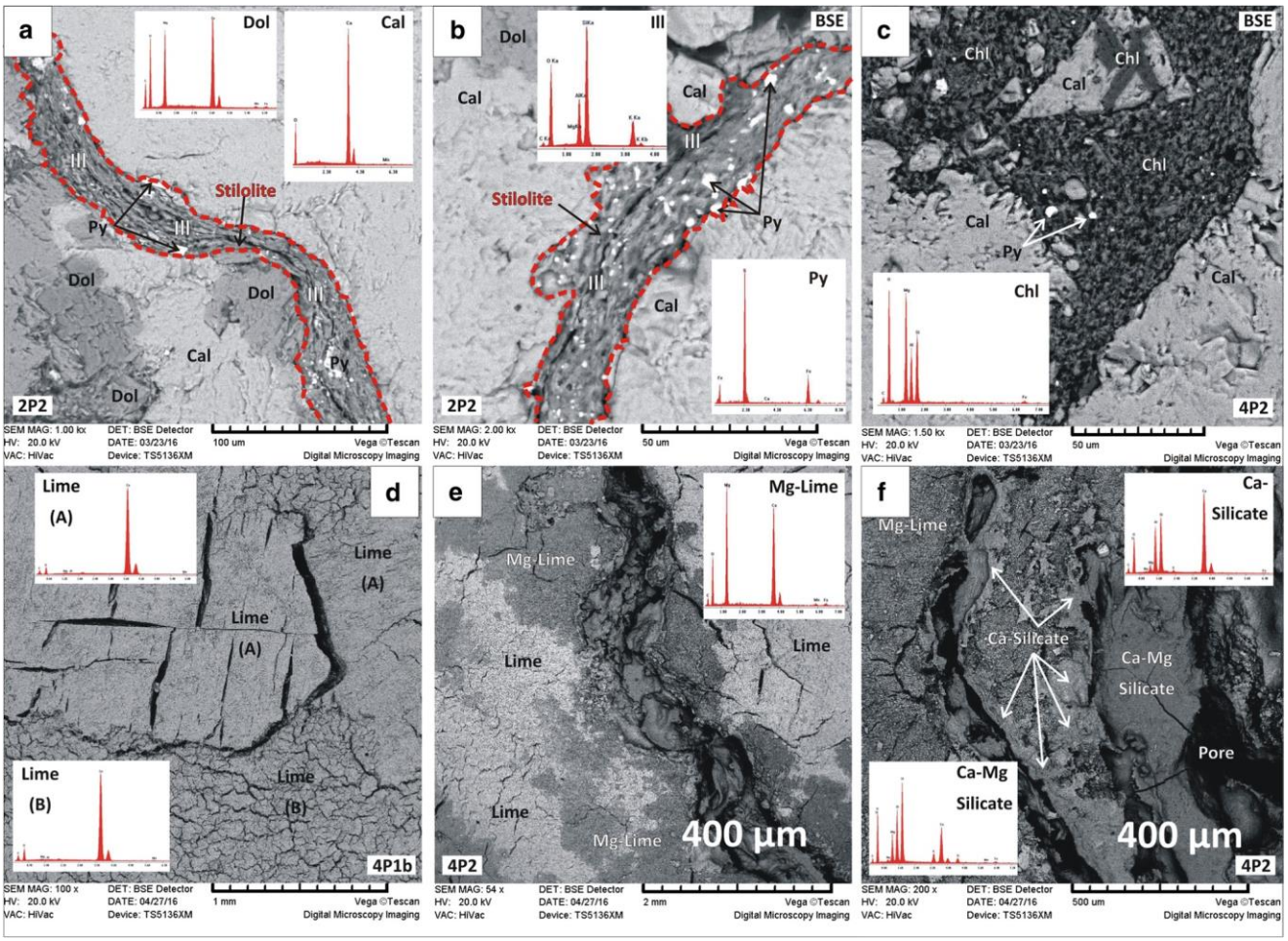

Fig. 6 Scanning electron microscopy (SEM-EDX) of limestone lime samples. Legend for mineral abbreviations: Cal: calcite; Dol:
and burnt lime samples along with stylolites. **a, b, c** Back scattered dolomite; Py: pyrite; Chl: clinochlore; Ill:
Illite images of limestone samples. **e, f, g** Back scattered images of burnt

Table 9 Results of numerical parameters from thermal analysis (TG-DTG)

Code	Unit	2P1	2P2	2P3	2P4	4P1a	4P1b	4P2
Starting time (t_1)	min	58.0	70.6	74.1	70.5	68.3	70.4	55.9
Ending time (t_2)	min	133.0	149.1	149.6	150.0	138.8	148.4	150.9
Max time (t_{max})	min	97.0	105.6	112.6	106.5	105.3	108.4	100.4
Δt (t_2–t_1)	min	75.0	78.5	75.5	79.5	70.5	78.0	95.0
Starting T (T_1)	°C	682.0	752.0	744.0	755.0	728.0	746.0	606.0
Ending T (T_2)	°C	1188.0	1195.5	1194.5	1197.0	1187.0	1194.0	1197.0
Max T (T_{max})	°C	1010.0	1020.0	1038.5	1032.0	1021.0	1026.0	993.0
ΔT (T_2–T_1)	°C	506.0	443.5	450.5	442.0	459.0	448.0	591.0

Symbols legend: *t* time, *T* temperature

4P2 and 4P3 are medium reactive (t_{60} = 5–6 min.), while samples 2P3, 2P4 and 4P1 are slowly reactive (t_{60} > 9 min.). A significant exception is represented by sample 2P1, which maintains a high reactivity (t_{60} < 2 min.) at 1150 °C. In any case, the average reactivity at 1150 °C is low (t_{60} = 7.4 min., T_{max} = 67.7 °C) (Table 11 and Fig. 8b). Either lime burnt at

1050 °C or at 1150 °C maintains a high available lime index (ALI ranges between 91.8 and 98.4% at 1050 °C; ALI ranges between 95.2 and 98.8% at 1150 °C, cf. Tables 10 and 11).

Variations of reactivity, plotted against the burning temperature, point out to an unusual and drastically pronounced sintering, or overburning tendency of the Neoarchean

Code	Unit	2P1	2P2	2P3	2P4	Weighted average 2P	4P1	4P2	4P3	Weighted average 4P
m-thick	m	2.0	2.1	3.9	2.1	–	14.9	2.7	0.4	–
Residual CO_2	Wt. %	0.46	0.41	0.40	0.06	–	0.17	0.5	0.5	–
$CaCO_3$ (calculated)	Wt. %	1.05	0.93	0.91	0.14	–	0.39	1.1	1.1	–
Total CaO (XRF-normalized)	Wt. %	93.1	98.3	93.6	96.0	95.0	98.3	89.4	99.7	97.0
Available lime index (ALI)	Wt. %	91.8	96.5	92.3	97.8	94.2	98.4	92.7	96.1	97.5
t_{60} (1050 °C)	min	0.81	1.37	1.74	0.82	1.3	1.24	4.00	0.97	1.6
T_{max} (1050 °C)	°C	73.0	66.9	65.4	71.8	68.5	73.6	62.8	77.0	72.1
T.A.S.T	min	5.5	5.0	4.5	4.0	4.7	3.5	6.0	6.0	3.9
Viscosity	–	Low	Low	Low	Low	–	High	Low	High	–

Code	Unit	2P1	2P2	2P3	2P4	Weighted average 2P	4P1	4P2	4P3	Weighted average 4P
m-thick	m	2.0	2.1	3.9	2.1		14.9	2.7	0.4	
Residual CO_2	Wt. %	0.2	0.4	0.0	ND		0.5	0.4	0.7	

Table 11 Results of technical tests on burnt lime samples at 1150 °C

$CaCO_3$ (calculated)	Wt.%	0.5	0.8	0.0	ND		1.2	0.8	1.6	
Total CaO (XRF-normalized)	Wt. %	95.3	98.3	94.5	97.6	96.1	98.1	92.7	95.5	97.2
Available lime index (ALI)	Wt. %	95.2	98.8	98.0	98.6	97.7	98.5	92.7	95.8	97.6
t_{60} (1150 °C)	min	1.8	6.8	17.5	9.4	10.5	11.3	6.1	7.3	10.4
T_{max} (1150 °C)	°C	70.3	67.3	62.0	64.5	65.3	65.2	63.9	70.4	65.1
T.A.S.T	min	6.0	10.5	11.5	11.0	10.1	16.5	8.5	12.5	15.2

ND not determined

limestone (Fig. 8c), with the exception of samples 2P1 and index (ALI) of each bench, has been calculated consider4P2, which present a similar reactivity either at 1050 °C or ing the thickness of each stratum. The average of technical at 1150 °C. tests performed at 1050 and 1150 °C is reported in Table 12.

The weight average of different technical parameters, These data have been used to calculate the influence of difincluding the reactivity (t_{60} and T_{max}) and the available lime ferent raw mixes feeding to kilns (Table 13).

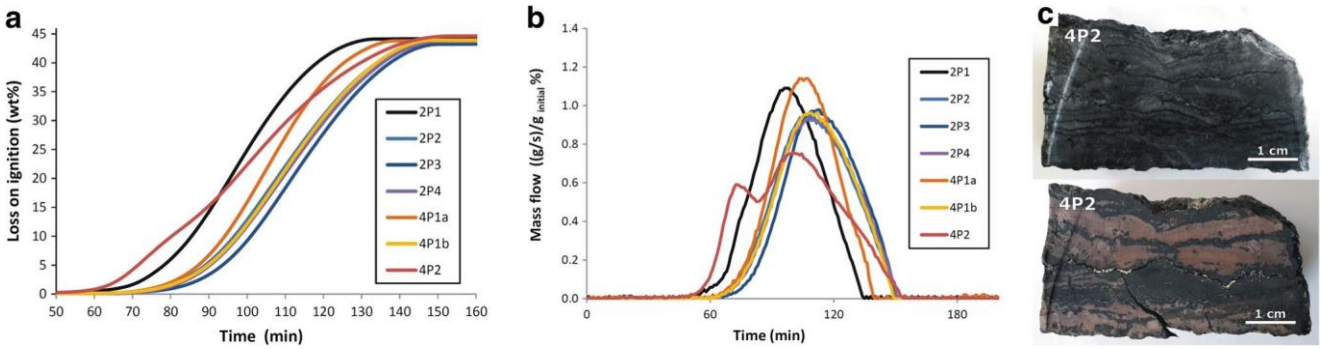

Fig. 7 Thermal analysis (TG-DTG) on limestone samples of the Ouplass Mine. **a** Loss ignition (%) vs. time (min.). This plot allows distinguishing calcination velocity of different samples. **b** Normalized Mass flow ([g/s]/$g_{initial}$)% vs. Temperature (°C). This plot allows distinguishing different lithology, especially sample 4P2 presents double **Table 10** Results of technical tests on burnt lime samples at 1050 °C reaction peaks, pointing out its dolomitic composition, while sample 2P1 presents the fastest thermal decomposition, i.e. calcination velocity (g/s). **c**: Visual comparison of the same prismatic chunk before and after the calcination at 1200 °C

Table 12 Technical tests on burnt limes (average of samples burnt at 1050 and 1150 °C)

Det.	Unit	Weighted average 2P	Weighted average 4P
Total CaO (XRF-normalized)	Wt. %	95.5	97.1
Available lime index (ALI)	Wt. %	96.0	97.5
Reactivity t_{60}	min	5.9	6.0
Reactivity T_{max}	°C	66.9	68.6
Reactivity T.A.S.T	min	7.4	9.6

Discussion

Depositional facies and diagenetic features

The Neoarchean limestone succession from the Ouplaas Mine is characterized by fenestrate and laminated microbial boundstone, associated with peloidal-intraclastic wackestone to packstone, and grainstone, deposited in a shallow subtidal to intertidal environment. Early marine carbonate cements consist of radial fibrous fans and herringbone calcite (Beukes 1980, 1987; Altermann and Schopf 1995; Sumner 1995, 1997a, 1997b; Sumner and Beukes 2006). Depositional textures are strongly affected by pervasive diagenetic recrystallization, which converted the micrite into microsparite, and equant and poikilotopic coarse sparite cements. The pervasive recrystallization is probably connected to the circulation of anchimetamorphic or hydrothermal fluids, often in contact with diabase intrusions, even if not directly observed in the mine. This fact is consistent with the Paleoproterozoic magmatism documented by Heaman (1997). Paragenetic pathways of carbonate minerals are broadly similar in all lithofacies with kerogen intimately associated with them. Organic carbon occurs as pigmentation in carbonate crystals, and as segregations of kerogen pigmentation around late diagenetic carbonate crystals and cavities (cf. Beukes et al. 1990). In marly limestones (samples 4P3 and 4P2, cf. Table 2, Figs. 3c, i and 4d–f), clasts are generally composed of kerogen pigmented laminated microsparite, which either floats in a matrix of fine-grained carbonate mud or is cemented by coarse sparite (Klein and Beukes 1989). According to Beukes et al. (1990), kerogen occurs in four major relationships with the carbonate minerals: (1) kerogen as pigmentation in microsparite, (2) kerogen and carbonate as reworked detritus, (3) kerogen as pigment segregated from calcite spar, and (4) kerogen displaced by carbonate. Some of the kerogen might be related to primary benthic microbial mats and appears to be a light brown pigment in the microsparite. Most of the kerogen observed in the studied samples seems to be strictly connected with the formation of stylolites and represents a thermally-mature late diagenetic graphitic carbon, which probably migrated into the carbonate deposit from another stratigraphically contiguous (or not-contiguous) source rock.

Limestone burnability and quicklime reactivity

Limestone microstructure and composition, depending from primary depositional features and diagenetic modifications, associated with the ancient geologic age of the rock, play a key role in controlling the kinetics of thermal decomposition, including the transfer of hot gases, and the escape of the CO_2 during the calcination process. These factors, as well as the burning temperature, control the microstructure of the neo-formed lime crystals in terms of grain growth, and BET specific surface area, and thereby the hydration rate of the slaking reactivity (t_{60}, T_{max}) (Eades and Sandberg 1970; Moropoulou et al. 2001; Kiliç and Mesut 2006; Hughes and Corrigan 2009; Soltan 2009; Soltan et al. 2011, 2012; Alaabed et al. 2014). In particular, previous studies have demonstrated that limestones with the lowest micrite to sparite ratio exhibit the lowest apparent activation energy value, the highest rate of calcination, and the highest lime reactivity (Vola and Sarandrea 2013; Marinoni et al. 2015). Effectively, the presence of euhedral-subhedral sparite crystals in the investigated Egyptian limestone enhances the formation of triple junction fractures, which also contribute to lowering the activation energy with accelerating lime liberation (Soltan and Serry 2011).

In the analyzed Neoarchean carbonates, the dominant micritic texture of the microbialite precipitates, even if interested by pervasive recrystallization, coupled with the presence of abundant organic carbon (kerogen), are key factors influencing the abnormally low burnability. Especially,

Table 13 Different scenarios showing the influence of different raw mixes on reactivity (t_{60} and T_{max}) and available lime index (ALI)

Scenarios	Raw mix	t_{60} (min.)	T_{max} (°C)	ALI	Notes
1	2P (100%)	5.9	66.9	96.0	The best raw mix for t_{60}
2	4P(100%)	6.0	68.6	97.5	The best raw mix for ALI and T_{max} (used from September to December 2013)
3	2P(65%) + 4P(35%)	5.9	67.5	96.5	Raw mix used from February to March 2014
4	2P(35%) + 4P(65%)	6.0	67.5	97.0	Natural quarry balance

Data are from the average of technical tests performed on bunt limes at 1050 and 1150 °C

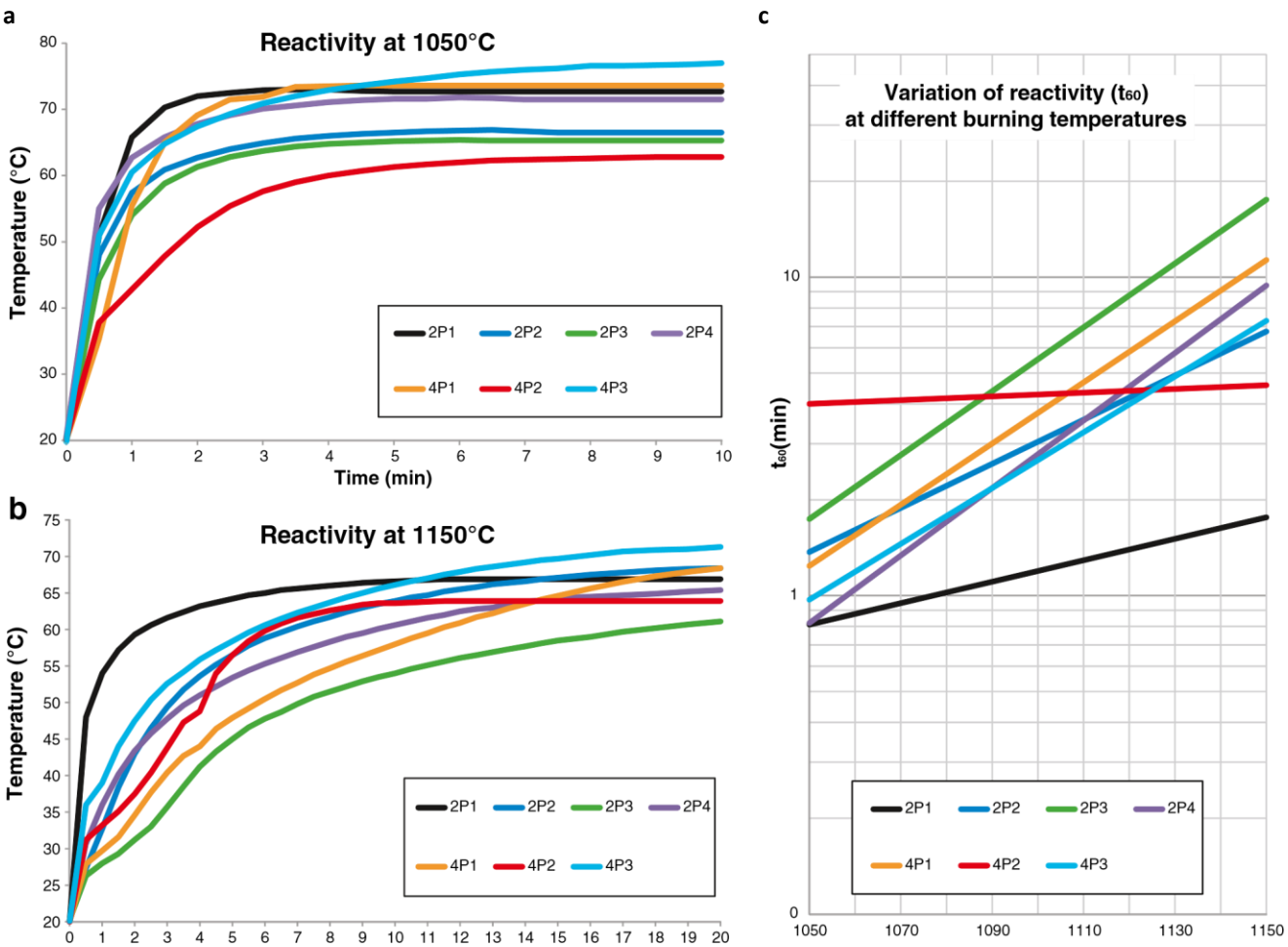

Time (min) Fig. 8 Reactivity tests according to standard EN 459-2. **a** Slaking curves of limes burnt at 1050 °C. **b** Slaking curves of limes burnt at 1150 °C. **c** Variations of reactivity (t_{60}) at different temperatures (1050 °C on the left and 1150 °C on the right) help in understanding

Temperature (°C)

the sensitivity to high temperature, and the sintering or overburning tendency of burnt lime samples in the restricted range of temperatures between 1050 and 1150 °C, with exceptions of sample 2P1 and 4P2

the low burnability is strictly related to the high sintering or overburning tendency and the low reactivity of the lime. Conversely, the presence of early marine herringbone calcite and late diagenetic burial cementation, i.e. the centimetersize poikilotopic calcite as in sample 2P1 (Figs. 3a and 4a–b), promotes a locally higher burnability and quicklime reactivity. In fact, sample 2P1 presents an earlier starting calcination temperature (t_1), a faster carbonate dissociation rate or calcination velocity (Δt) and a lower sintering tendency (see Table 9 and Fig. 7a–b). The evident sintering or overburning tendency of the studied Neoarchean limestone is well documented by the progressive darkening of the burnt lime at increasing burning temperature (Fig. 7c). This fact is combined with the progressive decay of the lime reactivity, while it doesn't affect the available lime index, which still remain high (Tables 10, 11 and Fig. 8). The typical brownish color of the lime is probably linked to the ubiquitous content of manganese-bearing minerals, probably microcrystalline braunite within the parental limestone, as shown in the back scattered electron maps obtained by means of the SEM-EDS analysis. Considering the temperature rise from the slaking tests (t_{60}) at 1050 and 1150 °C, it is possible to classify each sample of the Ouplaas Mine on the basis of its sensibility to the high temperature (Carmeuse 2014). A first group of samples, including 2P2, 2P3, 4P1 and 4P3, was identified which is very much sensitive to high temperature; conversely, a second group, including 2P1 and 4P2 samples, is not so much sensitive to high temperature (Fig. 8c).

In particular, sample 2P1 shows the highest reactivity either at 1050 °C or at 1150 °C (Tables 10, 11 and Fig. 8a–b). This result can be explained considering its different microfacies, presenting predominant fenestrate microbial boundstone (microbialite A), characterized by centimeter-sized cavities filled in by poikilotopic calcite (Figs. 3a and 4a–b). The highest reactivity of sample 2P1 is consistent with results from the thermal analysis, pointing out its highest velocity in thermal decomposition or calcination velocity (Δt), with respect to other samples, lacking the poikilotopic calcite (Table 9 and Fig. 8b).

Sample 4P2, which shows a medium reactivity either at 1050 °C or at 1150 °C, is not so much sensitive to high temperature as well as sample 2P1, but in this case, the impurity content, mostly represented by dolomite replacements, combined with the highest concentration of clay minerals, affects its reactivity (Tables 4, 5, 8, 10, and 11). Another factor affecting the limestone burnability could be the organic carbon (kerogen), which also burns during the calcination process.

In any case, considering that it is almost difficult, if not impossible, from the mining point of view, separating materials and strata with a lower technical quality belonging to the same bench, we just calculated the average weighted reactivity of benches 2P and 4P, on the basis of the thickness of each lithofacies assemblage (Figs. 2 and 3). Therefore it was possible estimating the impact of different lithofacies assemblage from each bench on burnt lime technical parameters (Tables 10, 11, and 12). Especially, we calculated four different scenarios, showing the impact of different quarry raw mixes on lime reactivity and available lime index (Table 13). Results show different raw mixes have a limited influence (ca. 0.1%) either on the ALI, or on the quicklime reactivity (t_{60}, T_{max}). In a particular way the highest reactivity of sample 2P1 has a limited effect because the thickness of the bottom stratum of the mine is limited, as well. For this reason it could be useful to evaluate a more consistent extraction of this stratum in the early future, by means of an in situ log survey, finalized to evaluate its real thickness below current quarrying level. More in general a deep geological survey of the mine, facilitate the determination of the real thickness and areal distribution of impure lithofacies, i.e. marly limestones and black shales, and to identify any dolomitization fronts. Geological and stratigraphic analysis, coupled with laboratory tests on raw materials from each stratum and bench of the mine, represent an essential approach to optimize the quality of the burnt lime product.

Conclusions

Considering the multidisciplinary analytical approach of this study, we traced the following conclusions:

1) The Neoarchean limestone from the Ouplaas Mine is very much sensitive to high burning temperatures showing an unusual and drastically pronounced sintering or overburning tendency. Especially, burnt lime presents a high reactivity at 1050 °C (t60 = 1.5 min., Tmax = 70 °C), but it rapidly decreases at 1150 °C (t60 = 9 min., Tmax = 65 °C). This fact can be better displayed plotting the reactivity against the burning temperature (Cf. Fig. 8c).
2) The unusual very low thermal behavior or burnability is strongly influenced by depositional textures, diagenetic history and secondly by presence of non-limestone impurities. Especially, the high sintering or overburning tendency and the low quicklime reactivity are related more to the micritic texture of the microbial boundstone, even if affected by diagenetic recrystallization into microsparite, rather than to the restricted presence of non-carbonate mineral contaminations.
3) The sample 2P1 represents the most significant exception. It shows characteristic marine herringbone calcite associated with late diagenetic burial cementation, i.e. the centimeter-size poikilotopic calcite. This sample presents the highest carbonate dissociation rate or calcination velocity and the least sensitivity to the high temperature, and thus the highest quicklime reactivity either at 1050 °C (t60 = 0.8 min., Tmax = 73 °C) or at 1150 °C (t60 = 1.8 min., Tmax = 70.3 °C).
4) The sample 4P2 is also not so much sensitive to high temperature, but its quicklime reactivity is medium either at 1050 °C (t60 = 4 min., Tmax = 62.8 °C) or at 1150 °C (t60 = 6 min., Tmax = 63.9 °C), because strongly affected by its impure composition, i.e. diagenetic replacive dolomite and clay minerals.
5) The presence of locally concentrated dolomitic marly limestones, back shales, an organic carbon (kerogen), negatively affects the quicklime reactivity because significantly lowers the available lime index, moreover kerogen burns during the heating process, facilitating the sintering or overburning tendency.

According to these observations, we also proposed to the customer perform the following useful actions:

1) To perform a deep geological survey of the mine stratigraphy, finalized to the correct determination of the real thickness of the impure strata, to identify dolomitization fronts and impurity distribution to optimize the quality of the extracted stone.
2) To perform an in situ log survey, finalized to evaluate the real thickness of the bottom stratum of the mine (2P1) below the current quarrying level, to evaluate the feasibility of its more consistent extraction in the early future.

The detailed knowledge of the mine stratigraphy, combined with the technical characterization of each stratum, allows calculating the real average weighted reactivity of each bench, and subsequently, the expected reactivity of different raw mixes feeding to the TSR kilns. This multidisciplinary approach must be repeated on more representative volumes of material extracted over the months and the years to validate the above results. If the higher reactivity of bench 2P will be validated by a massive campaign of tests, it could be successfully adopted to improve the raw mix feeding to the kilns, depending on the target parameter required by the customer. The judicious selection of raw material from different benches of mines could also reduce the negative influence of strata with a higher overburning tendency, and/or with a lesser compositional quality.

References

Alaabed S, Soltan MA, Abdelghany O, Amin BEM, Tokhi ME, Khaleel A, Musalim A (2014) United Arab Emirates limestones: impact of petrography on thermal behaviour. Mineral Petrol. https://doi. org/10.1007/s00710-014-0329-3

Altermann W, Schopf JW (1995) Microfossils from the Neoarchean Campbell group, Griqualand west sequence of the Transvaal Supergroup, and their paleoenvironmental and evolutionary implications. Precambrian Res 75:65–90

Altermann W, Wotherspoon JMCD (1995) The carbonates of the Transvaal and Griqualand west sequences of the Kaapvaal Craton, with special reference to the lime acres limestone deposit. Miner Deposita 30:124–134

ASTM C25 (2011) Standard test methods for chemical analysis of limestone, quicklime, and hydrated lime. ASTM Book Stand
04.01:28–30

Beukes NJ (1980) Lithofacies and stratigraphy of the Kuruman and Griquatown iron-formations, northern Cape Province, South Africa. Trans Geol Soc S Afr 83:69–86

Beukes NJ (1984) Sedimentology of the Kuruman and Griquatown iron-formations, Transvaal Supergroup, Griqualand West, South Africa. Precambrian Res 24:47–84

Beukes NJ (1987) Facies relations, depositional environments and diagenesis in a major Early Proterozoic stromatolitic carbonate platform to basin sequence, Campbellrand Subgroup, Transvaal Supergroup, Southern Africa. Sediment Geol 54:1–46

Beukes NJ, Klein C, Kaufman AJ, Hayes JM (1990) Carbonate petrography, kerogen distribution, and carbon and oxygen isotope variations in an early Proterozoic transition from limestone to ironformation deposition, Transvaal Supergroup, South Africa. Econ Geol 85:663–689

Bish DL, Howard SA (1988) Quantitative phase analysis using the Rietveld method. J Appl Cryst 21:86–91

Boynton RS (1980) Chemistry and technology of limes and limestone, 2nd edn. Wiley, p 159–191

Button A (1973) The stratigraphic history of the Malmani dolomite in the eastern and north-eastern Transvaal. Trans Geol Soc S Afr 76:229–247

Carmeuse (2014) Idwala South Africa, KFS calcination tests, Stone committee. Confidential Internal Report 1–25

Cheng C, Specht E (2006) Reaction rate coefficients in decomposition of lumpy limestone of different origin. Thermochim Acta 449:8–15

Chilingar GV (1960) Notes on classification of carbonate rocks on basis of chemical composition. J Sediment Res 30:157–158

Dunham RJ (1962) Classification of carbonate rocks according to depositional texture. AAPG Mem 1:108–121

Eades JL, Sandberg PA (1970) Characterization of the properties of commercial lime by surface area measurements and scanning electron microscopy. ASTM STP 472:3–24

Elsen J, Mertens G, Snellings R (2011) Portland cement and other calcareous hydraulic binders: history, production and mineralogy. In: Christidis GE (ed) Advances in the characterization of industrial minerals. EMU, London 9(11), p 441–479

Embry AF, Klovan JE (1971) A Late Devonian reef tract on Northeastern Banks Island. Bull Can Petrol Geol 19:730–781

Emmerich K (2011) Thermal analysis in the characterization and processing of industrial minerals. In: Christidis GE (ed) Advances in the characterization of industrial minerals. London, 9(11): 129–170

EN 459-2 (2010) Building lime - Part 2: test methods. CEN, p 72–84 Flügel E (2004) Microfacies of carbonate rocks. Springer

Friedman GM (1965) Terminology of recrystallization textures and fabrics in sedimentary rocks. J Sed Petrol 35:643–655

Frolova EK (1959) On classification of carbonate rocks of limestonedolomite-magnesite series. Novosti Neft Tekhn, Geol 3:34–35

Galimberti M, Marinoni N, Della Porta, Marchi M, Dapiaggi MG (2016) Effects of limestone petrography and calcite microstructure on OPC raw meal burnability. Miner Petrol. https://doi. org/10.1007/s00710-016-0485-8

Grotzinger JP (1989) Facies and evolution of Precambrian carbonate depositional system: emergence of the modern platform archetype. In: Crevello P, Read JF, Sarg R, Wilson J (eds) Controls on carbonate platform and basin development. Soc Econ Paleont Mineral 44:79–106

Grotzinger JP, James NP (2000) Precambrian carbonates; evolution of understanding. In: Grotzinger JP, James NP (eds) Carbonate sedimentation and diagenesis in the evolving Precambrian world. SEPM 67:3–20

Gunasekaran S, Anbalagan G (2007) Thermal decomposition of natural dolomite. Bull Mater Sci 30:339–344

Heaman LM (1997) Global mafic magmatism at 2.45 Ga: remnants of an ancient large igneous province? Geology 25:299–302

Hughes JJ, Corrigan M (2009) Microstructural expression of temperature and residence time in laboratory calcinated limestone. Proc. 12th EMABM, Dortmund, p 328–334

Kiliç Ö, Mesut A (2006) Effects of limestone characteristics properties and calcination temperature on lime quality. Asian J Chem 18:655 – 606

Klein C, Beukes NJ (1989) Geochemistry and sedimentology of a facies transition from limestone to iron-formation deposition in the early Proterozoic Transvaal Supergroup, South Africa. Econ Geol 84:1733–1742

Larson AC, Von Dreele RB (1994) General structure analysis system (GSAS). Los Alamos National Laboratory Report LAUR, p 86–748

Marinoni N, Allevi S, Marchi M, Dapiaggi M (2012) A kinetic study of thermal decomposition of limestone using in-situ high temperature X-ray powder diffraction. J Am Ceram Soc 95:2491–2498

Marinoni N, Bernasconi A, Della Porta G, Marchi M, Pavese A (2015) The role of petrography on the thermal decomposition and burnability of limestones used in industrial cement clinker. Miner Petrol 109:719–731

Miyano T, Beukes NJ (1984) Phase relations of stilpnomelane, ferriannite, and riebeckite in very low-grade metamorphosed ironformations. S Afr J Geol 87:111–124

Moropoulou A, Bakolas A, Aggelakopoulou E (2001) The effects of limestone characteristics and calcinations temperature to the reactivity of the quicklime. Cem Concr Res 31:633–639

Paris G, Adkins JF, Sessions AL, Webb SM, Fischer WW (2014) Neoarchean carbonate–associated sulfate records positive Δ33S anomalies. Science 346(6210):739–741

Sibley DF, Gregg JM (1987) Classification of dolomite rock textures. J Sed Res 57(6):967–975

Soltan AM (2009) Petrographic modelling of Egyptian limestones for quicklime production. Arabian J Geosci 4:5–6. 803–815

Soltan AM, Serry MA-K (2011) Impact of limestone microstructure on the calcination activation energy. Adv Appl Ceram 7:409–416

Soltan AM, Kahl W-A, Hazem MM, Wendschuh M, Fischer RX (2011) Thermal microstructural changes of grain-supported limestones.
Mineral Petrol 130:9–17

Soltan AM, Kahl W-A, Wendschuh M, Hazem M (2012) Microstructure and reactivity of calcined mud supported limestones. Miner Process Extr Metall 121:5–11

South African Committee for Stratigraphy (SACS) (1980) Stratigraphy of South Africa, part 1. In: Kent LE (ed) Litho-stratigraphy of the Republic of South Africa, South West Africa/Namibia, and the Republics of Bophuthaswana, Transkei and Venda. Handbook
Geol. Surv. S. Afr. 8, p 1–690

Sumner DY (1995) Facies, paleogeography, and carbonate precipitation on the Archean (2520 Ma) Campbellrand-Malmani Carbonate Platform, Transvaal Supergroup, South Africa. MIT, Ph.D. 9/1995, p 1–514

Sumner DY (1997a) Carbonate precipitation and oxygen stratification in late Archean seawater as deduced from facies and stratigraphy of the Gamohaan and Frisco formations, Transvaal Supergroup, South Africa. Am J Sci 297:455–487

Sumner DY (1997b) Late Archean calcite-microbe interactions: two morphologically distinct microbial communities that affected calcite nucleation differently. Palaios 12:302–318

Sumner DY, Beukes NJ (2006) Sequence stratigraphic development of the Neoarchean Transvaal carbonate platform, Kaapvaal Craton,
South Africa. S Afr J Geol 109(1–2):11–22

Sumner DY, Bowring SA (1996) U-Pb geochronologic constraints on deposition of the Campbellrand Subgroup, Transvaal Supergroup, South Africa. Precambrian Res 79:25–36

Sumner DY, Grotzinger JP (1996) Herringbone calcite: petrography and environmental significance. J Sediment Res 66:419–429

Sumner DY, Grotzinger JP (2000) Late Archean aragonite precipitation: petrography, facies associations, and environmental significance. In: Grotzinger JP, James NP (eds) Carbonate sedimentation and diagenesis in the evolving Precambrian world. SEPM 67:123–144

Sumner DY, Grotzinger JP (2004) Implications for Neoarchaean ocean chemistry from primary carbonate mineralogy of the Campbellrand-Malmani Platform, South Africa. Sedimentology 51:1–27

Toby BH (2001) A graphical user interface for GSAS. J Appl Crystallogr 34:210–213

Tucker M, Wright VP, 1990. Carbonate sedimentology. Blackwell Science

Vola G, Sarandrea L (2013) Raw materials characterization for industrial lime manufacturing. ZKG Int 66(5):62–70

Vola G, Sarandrea L (2014) Lime reactivity study. World Cem 45(6):49–55

Walraven F, Armstrong RA, Kruger FJ (1990) A chronostratigraphic framework for the north-central Kaapvaal Craton, the Bushveld complex and the Vredefort structure. Tectonophysics 171:23–48

Whitney DL, Evans BW (2010) Abbreviations for names of rock-forming minerals. Am Min 95:185–187

Young RA (1993) The Rietveld method. University Press, Oxford